Rot Detection in Wooden Poles using Electrical Impedance Tomography

Fayaaz Ali Sattar

Supervised by:

Dr. Andrew John Wilkinson

A dissertation submitted to the Department of Electrical Engineering,
University of Cape Town, in fulfilment of the requirements
for the degree of Master of Science in Engineering.

Cape Town, November 2005

Declaration

I declare that this dissertation is my own, unaided work. It is being submitted for the degree of Master of Science in Engineering in the University of Cape Town. It has not been submitted before for any degree or examination in any other university.

Signature of Author . Signed by candidate .....

Cape Town

1 November 2005

Abstract

The proposal for this dissertation was to develop a nondestructive method of testing wooden utility poles for rot and termite damage. The nondestructive method that was chosen for this project was that of electrical impedance tomography in which an image of the permittivity in a cross section would be created from impedance measurements made between electrodes attached to the boundary of the pole.

Rot and termite damage in wooden utility poles has been an ongoing problem. The electricity and telecommunication companies making use of such poles have a duty in order to assure supply of their product as well as the safety of the public in the vicinity of the poles. Most of the wooden poles do not have a fixed lifespan as some are in dry conditions and some in wet. Due to the variation in longevity, the replacement of all the wooden poles over a certain age would prove to be too expensive. This report will try and develop a method in which the utility companies can measure the amount of decay within the wooden poles. This would then assist a company in determining which wooden poles need to replaced.

The literature survey suggested that an AC based capacitance tomography system would suite the needs of our system. The AC based capacitance system was modified in order to extract an impedance measurement. Due to the minute magnitude of the measurements the design of the circuitry had to be ultra sensitive to small changes in capacitance. The typical measurement for two electrodes $180mm$ apart was within the femto Farad range, 10^{-15}, if we considered only the capacitance part of the impedance measurement. The circuitry consisted of a flow of the measured information starting from the conversion of the measured signal into a measurable voltage. This measured voltage then need to be amplified for further use. The amplified signal was then demodulated into its real and imaginary components for a complete impedance measurement. The demodulated signal was then fed into a computer for analysis. Each electrode has its own measurement channel. This allowed us to measure the signals in parallel. In an N electrode system, if we drive on one electrode, we can measure the signals on the other $N - 1$ electrodes. The thesis contains detailed sections outlining each step of the measurement process with reference to component considerations, mathematical analysis and design. The results was an impedance measuring transducer capable of measuring extremely small capacitances. The whole system is controlled via a PC data acquisition card. This involved the controlling of driving electrodes, the creating of the driving signal, the switching of the phase

synchronous detection with reference to I and Q and the capturing of the data from the measuring channels.

A capacitance tomography image reconstruction algorithm was used to reconstruct an image of the electrical permittivity in a planar cross section.

In order to test the system for the detection of rot we used a three step process. Initially a perspex jar was used for testing. This involved strapping the electrodes around the circumference of the jar. For each reconstruction a calibration and offset dataset is needed. Objects were placed within the calibrated air space of the perspex jar. The results showed that objects of varying permittivity could easily be detected. The measurement system was tested with a variety of objects including plastic rods, $50mm$ wooden poles, glycerol and water. All the images produced, accurately showed the insertion of the objects. The second step of the process involved strapping the electrodes around a machined wooden pole (diameter $180mm$) used for timber construction. The machined wooden poles were given to a workshop to drill $50mm$ and $100mm$ holes through the center. These holes were used to simulated rot. Poles of the same diameters ($50mm$ and $100mm$) were bought in order to fill the simulated rot. This enabled us to calibrate the system without having to shift the electrodes. The results shown from the simulated rot were excellent.

The final process involved the testing on actual wooden pole samples from the field. The samples that we used had a healthy section and a rotten section. We strapped the electrodes around the healthy section in order for calibration. Due to the fact that the real samples had knots and bumps on the surface the shifting of the electrodes to the rotten section resulted in some misalignment of the electrodes. This made the results less accurate than those obtained for the simulated rot but none the less clearly showed us the rotten portions.

In conclusion we have proved that the system is capable of detecting presence of rot in wooden utility poles.

Finally, the major recommendation is that a testing rig needs to be developed in order to prevent electrode misalignment when testing real poles. This would significantly improve the performance.

Acknowledgements

This thesis would not have been possible without the help and support of the following people. My supervisor, Andrew John Wilkinson, for always assisting me whenever I encountered a problem. I would also like to thank him for his patience and time during the difficult parts of the project as well as his great debugging skills. I would like to thank the NRF for a grant holder linked bursary. I would like to thank the UCT University Research Committee and Eskom Tesp for my bursary top ups. I would like to thank Prof. T. Gaunt for bringing the pole rot problem to the attention of our research group and for arranging a literature survey to be undertaken for Eskom. I would like to thank my mother, Amina Sattar, who assisted me with the sewing required to creating the Velcro elastic band used to hold up the electrodes. I would like to thank Zunaid Parker who assisted me in the mathematical and programming areas of the project. I would like to thank the mechanical and electrical workshops for giving me the equipment and assistance I needed to construct the various devices. I would like to thank Bill Randall for assisting me in the layout and development of the PCB.

Contents

List of Figures

Nomenclature

Admittance— is the reciprocal of impedance. $Y = 1/Z = G + jB$, where G = conductance, and B = susceptance.

ADC— Analog to digital converter.

Electrical Conductance— is the reciprocal of electrical resistance. It is a measure of how easily electricity flows along a certain path through an object. [3]

DAC— Digital to analog converter.

DAQ— Data acquisition card.

Device Under Test (DUT)— The object under which the test is being held.

Dielectric Constant— is the ratio of the amount of electrical energy stored in an insulator, when a static electric field is imposed across it, relative to vacuum (which has a dielectric constant of 1). Thus, the dielectric constant is also known as the static permittivity. [3]

Electrical Capactance Tomography (ECT)— is a method by which a series of capacitive measurements are taken around a DUT in order to reconstruct an image.

Electrical Impedance Tomography (EIT)— is similar to ECT but includes a full impedance measurement.

Eskom— South African electricity utility company.

GBP— Gain bandwidth product is a parameter that indicates the maximum possible product of gain and bandwidth.

I— Signifies an inphase signal.

Impedance— is a measure for the manner and degree a component resists the flow of electrical current if a given voltage is applied. Technically speaking, it is the combined effect of capacitance, inductance, and resistance on a signal.

Q— Signifies the quadrature signal relative to the inphase signal.

Chapter 1

Introduction

1.1 Background to Research

The problem of rot in wooden utility poles has been an ongoing problem for electricity distribution companies across the world. These wooden poles are used as the main method of carrying electricity lines for distribution among urban areas. After a certain period of time the wood becomes susceptible to rot due to weathering and the absorption of water at ground level. This problem only occurs to a certain number of poles in a distribution line. The problem faced by the distribution companies is to accurately determine which of these poles are rotting and how long a life span they still have. The problem of testing these poles for rot lies in the method of testing. Several methods use invasive techniques to determine the state of the pole, this would involve some kind of penetrating object to probe the core of the pole to extract samples or determine its density. By using an invasive technique to test the pole we could possibly be decreasing its lifespan further. The hole created by the invasive technique, if not sealed properly, could serve as a channel in which further rot could spread and therefore cripple the pole

In an aim to prevent the invasive testing of wooden poles this research project was developed. The project scope was to find alternative means of testing the wooden poles non-invasively. The main focus of this dissertation is the development of a impedance tomography system that would be sensitive enough to measure wood rot. An impedance tomography system would be a non-invasive means of testing, as the measurements are taken across electrodes that does not need to be in-direct contact of the wooden pole.

A problem of this scale would have major impact on both the utility companies and the environment. Utility companies would save money by not having to replace all or most of the poles within a distribution line if they have been tested healthy. There would also be a long term impact on the environment in that there would be less demand for timber to construct these distribution lines.

1.2 Plan of Development

The thesis will develop from a literature survey of the existing methods of testing wooden poles. These methods will be analysed and identified as invasive, unsatisfactory or beneficial to our further studies. We will then take a closer look at the studies involving capacitance tomography including the different methods of measuring capacitance and its sensitivity. In chapter 3 we will use the information about capacitance tomography to lay the base for the design of our impedance tomography system. The thesis will give detailed information about the design aspects involved in developing the measurement circuitry, with consideration to component choices, noise calculations, data acquisition, synchronous detection and multiplexing. In chapter 4 an overview is given of the technical difficulties experienced putting these design aspects to test. This will be followed by some of the practical aspects related to the design followed by the initial testing of the board. This will be followed by the the findings chapters. The findings chapters will be divided into two separate chapters. Chapter 5 in which the system's sensitivity to various object including non wooden objects we be tested and Chapter 6 in which the findings on the actual testing on wooden poles. This would be followed by the conclusions and recommendations.

Within this thesis we will try to prove that the method proposed will indeed reveal that rot will be detectable using electrical impedance tomography.

Chapter 2

Literature Survey

In this chapter we will review the previous and current methods being used to detect rot in wooden poles. We will also review the current work being done in the field of capacitance tomography, and the different methods of producing a capacitance measuring transducer.

2.1 Existing methods and apparatus used for pole condition monitoring

A literature scan was done in order to research the previous methods which had been applied to this problem. The scan involved the use of various databases and search engines. The common words used in these searches were *wood, utility, non-destructive, testing, tomography, rot, inspection, examination and poles*. The results provided information about current research methods as well as commercial products that are currently available. These methods are products are described in the following sections.

2.1.1 Eskom pole testing standard (SCSASAAX2)

The Eskom, the South African electricity utility company, standard [5] describes the presently employed method of maintenance and inspection of wooden utility poles in South Africa. The standard is a guide on how to inspect a utility pole. The standard requires a qualified inspector to be present for the inspection of the poles. An inspector is only considered qualified once he has inspected 1000 poles under the direct supervision of a qualified inspector. The inspection involves the gathering of a series of external information such as pole number, species, soil compactness, lightning damage, extreme cracks, visible rot and pole twisting to name a few. Once the external pole has been inspected an area around the pole in excavated to a depths of 250mm. The internal inspection of the pole involves the drilling of two 12mm holes at 45^o angles to the ground as shown in figure 2.1. One hole is drilled 100mm below ground and the other at ground level. A tool designed specifically to extract wood fibre is inserted into each hole drilled to probe for

incipient decay and hence determine the thickness of the shell.

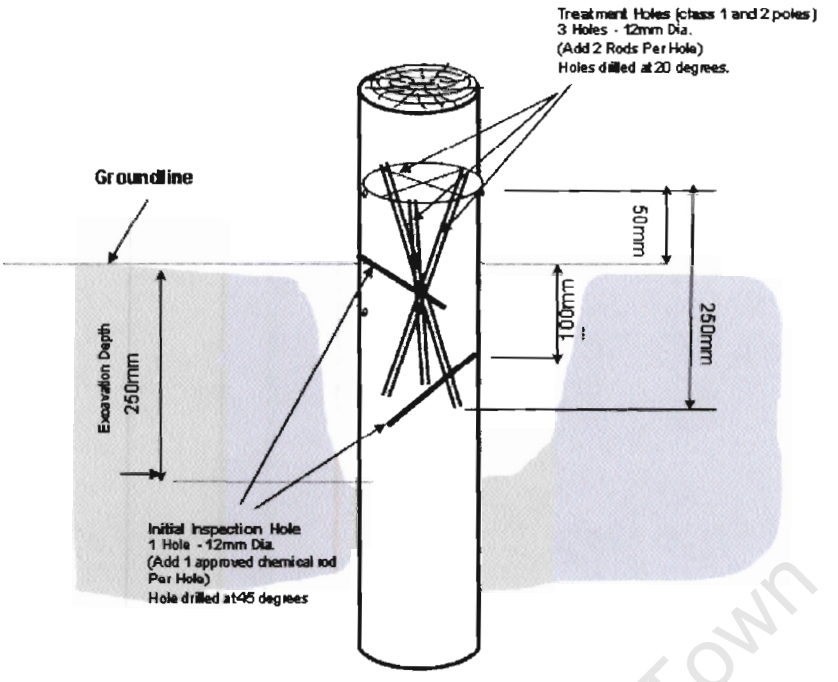

Figure 2.1: Diagram of inspection drilling points including chemical treatment drilling points [5]

The inspector uses his expertise and all this information to classify the poles into one of four classes ranging from sound pole to major damage. A suitable remedial treatment may be given to the poles depending on their classification. This normally involves treating the pole with chemicals internally as well as externally depending on the extent of the damage. The more heavily damaged poles are given additional reinforcement with stubbing. Stubbing is the process whereby a short wooden pole or approved steel staking system is attached to a class 3 pole, giving it the required load strength of a new pole. Class 4 poles have to be replaced within six months of the inspection. After the treatment each pole is marked with the class and treatment it received.

Although the Eskom standard is a very thorough inspection method, it still involves a destructive method of testing the poles. The 12mm drill holes are filled and plugged but would probably still leave the pole more susceptible to future rot. A lot of the inspection also depends on the experience of the inspector which could possibly lead to human error at times.

2.1.2 The Resistograph

The Resistograph is produced by IML Inc[16]. The instrument is a portable battery operated drilling mechanism for detecting voids in wooden poles.

The resistograph detects defects in wood using a pressure sensitive drill tip. The instrument is applied to the wooden pole and a trigger allows a drill bit with a diameter of

1.5mm to enter the pole at a constant rate. The pressure sensitive measurement of the wood is then printed on a portable printer supplied with the instrument giving a sensitivity reading as the drilling occurs. A void in the pole would be recognized as a dip in the graph, symbolizing no pressure on the tip, as shown in figure 2.2.

Figure 2.2: Resistograph Measurement showing decay [16]

This sort of method is still classified as invasive as a drill has to penetrate the pole in order to get information about its strength. Also the information retrieve from the sensitivity measurement is only for a single drill through a cross section. This can leave a false sense of strength by not being able to detect none central voids as shown in figure 2.3.

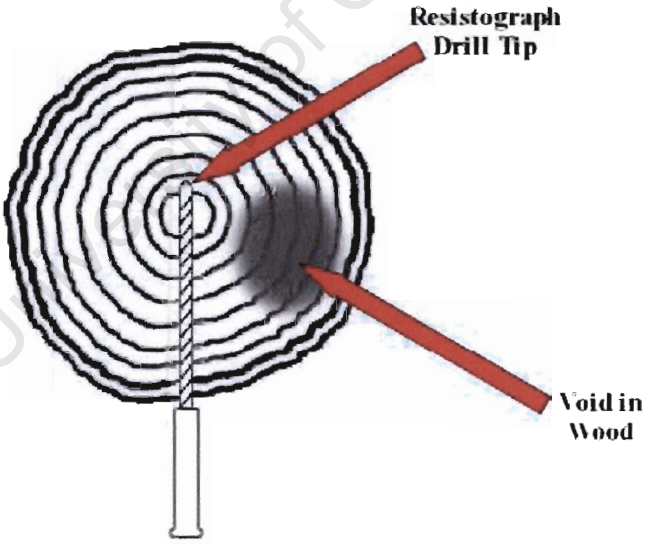

Figure 2.3: Diagram of possible false reading on Resistograph

2.1.3 Polux

Polux from CBS-CBT[2] was developed in conjunction with EDF (Electricité de France) and EPFL

(Ecole Polytechnique Fédérale de Lausanne, Schwitzerlandin). Polux measures two parameters in wooden poles to determine its durability. It measures the density and the moisture by driving in two pins at the base of the pole as shown in figure 2.4.

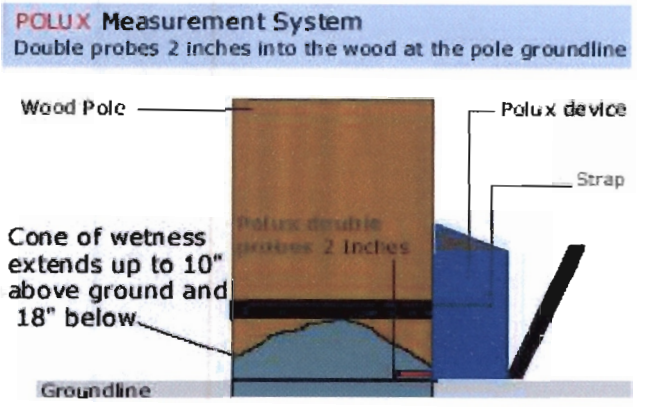

Figure 2.4: Diagram of Polux instrument strapped to a pole [10]

The instrument is strapped to the pole and a lever behind it is use to drive in the pins. The driving in of the pins is used to measure the penetration resistance. Once the pins are within the poles the moisture measurements are then taken. The pins are driven in at two points as shown in figure 2.5. The combinations of these two measurements are used to determine the state and durability of the pole. The device needs to be calibrated with respect to the wood species that the company uses to manufacture their utility poles.

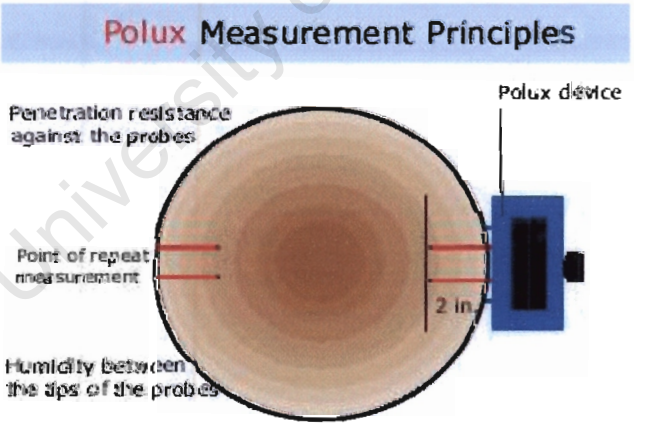

Figure 2.5: Two measurement position using Polux [10]

As we can see from figure 2.5, the measurements only cover a certain area of the pole, leaving for some room of failure. It also drives two pins into the pole at ground level, the level at which the pole is most susceptible to rot due to moisture. Even with plugging the pole now stands a greater risk of infestation or rot.

According to an Eskom survey [20], the Polux only failed 3 poles where the Eskom standard (SCSASAAX2) failed 26 poles in the same utility pole line. By failing a pole we

mean that it is unfit for future reliable use. These failure could be attributed to the measurements the instrument uses to classify healthy and unhealthy poles. The Polux only measured the hardness of the pole around the boundary at ground level, so even if the pole had rot it would pass it if it was sufficiently hard on the outer rim.

2.1.4 Mechanical Bending Methods

There are various researched mechanical methods [22] of determining pole strength. One of these methods involve using bending moments and the modulus of elasticity. The testing is normally done by attaching a large mechanical device to the pole. This is a normally a three pointed device that has one point anchored at the base of the pole as shown in figure 2.6. The device then exerts pressure onto the base of the pole giving us a reading of its bending moment.

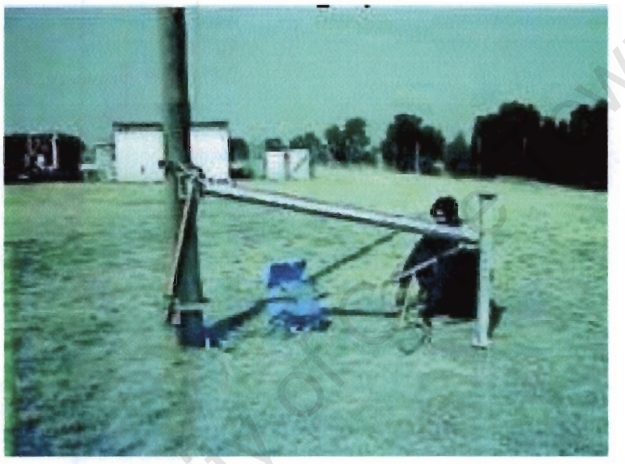

Figure 2.6: TSI Mechanical pole tester [7]

The pressure is steadily applied by a hydraulic pump increasing the bending moment which increases the deflection. This is done until a predetermined maximum bending moment. The measured deflection for a particular bending moment is then plotted against each other and compared to a precalculated graph of the poles strength known as the safe bending moment. To produce this graph a series of information about the pole is used in order to calculate the wind force on pole factor. To calculate this the following information is required:

- Conductor diameter
- Number of conductors
- Length of the pole
- Planting depth
- Span length
- Diameter of the pole

Once the wind force on the pole and the conductor has been calculated its safe bending moment can then be determined. The safe bending moment can then be compared to the bending moment measured by the device. If the measured bending moment is less than the safe bending moment for particular deflection then the pole is classified as healthy.

This method is non-invasive but requires a lot of information about the pole and it requires one to operate cumbersome equipment in order to obtain the necessary information for analysis.

2.1.5 DE-K Tector

The DE-K Tector [23, 14] is a portable battery operated device manufactured by Heath Consultants of Houston Texas. It is used to detect decay in wood using a sonic hammer, measuring transducer and a metering device. The hammer is used to knock the wood while the transducer is placed on the opposite side to measure the effects of the travelled sound as shown in figure 2.7. The measured signal is passed through two band pass filters (one isolating higher frequency components and the other the lower frequency components [23]). It works on the simple principle that decayed wood absorbs more high sonic frequencies than healthy wood. The device is non-invasive but it is not a direct measurement of the strength of the wood but a linear measurement for the detection of decay.

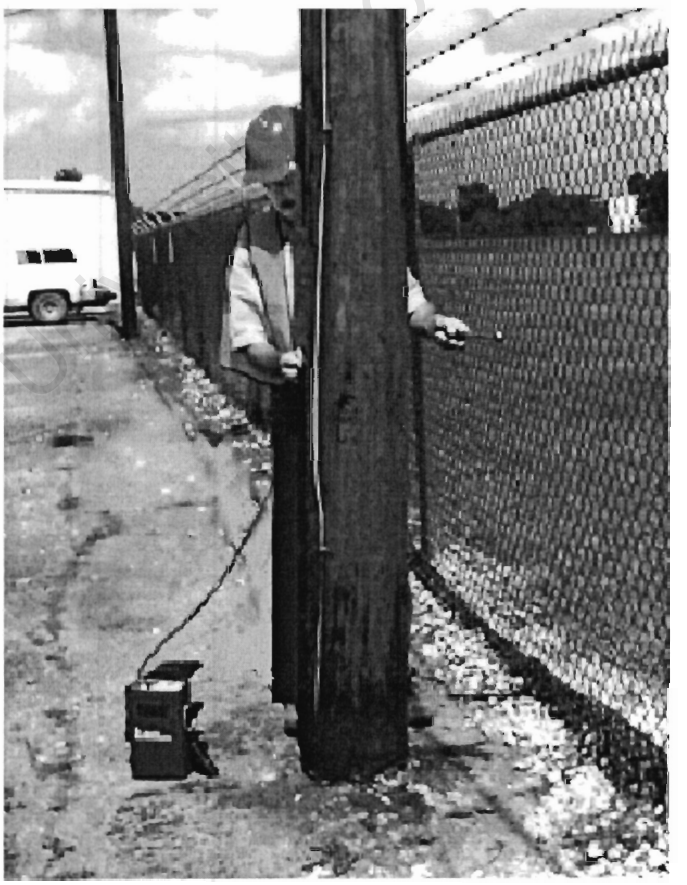

Figure 2.7: Pole under test using DE-K Tector [14]

2.1.6 Ground Penetrating Radar (GPR)

A GPR method has been developed by a Canadian Firm, Sensors and Software Inc. [25]. The system uses a pulseEKKO 1000 GPR system which can reproduce length based profiles of wooden poles. The pulseEKKO operated with 1200 MHz antennas. The system works as traditional radar, transmitting a signal into the wood and recording the time for the return echo. Not a lot of information about the operation and technical aspects of the device is given by the company. Images of the device in use and reconstructed images can be seen in figures 2.8 and 2.9.

Figure 2.8: GPR device in use with an extracted wooden pole [25]

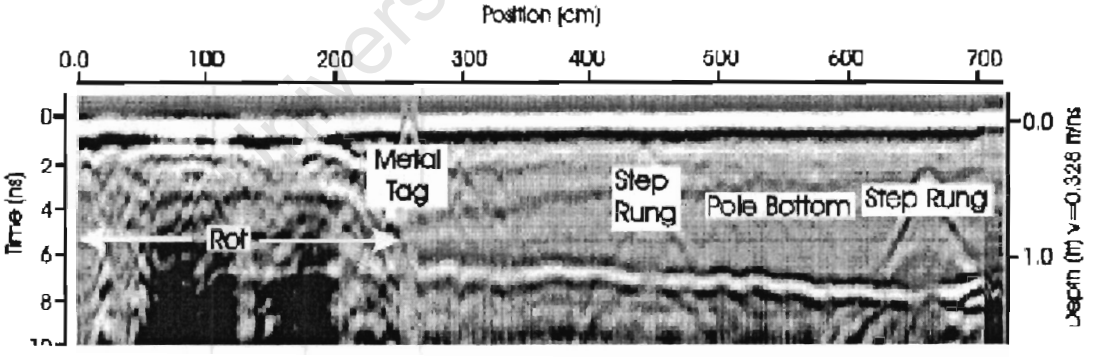

Figure 2.9: GPR scan of a tree showing the indication of rot [25]

2.1.7 PURL - Pole Ultrasonic Rot Locator

PURL is manufactured in the UK by EA Technology LTD [18]. The PURL system consists of a hand held ultrasonic transmitter and receiver as well as the necessary software needed to determine the state of the pole. The transmitter is used to propagate signals through the pole and into the receiver. The system works on the principle that signals get

attenuated through decay or rotten wood. The transmitter is screwed into the pole while the receiver is firmly pressed against the pole to measure the received signal as shown in figure 2.10.

Figure 2.10: PURL system in use [18]

The method of testing involves screwing in the transmitter into the base of the pole for good propagation of the signal into the wood. The receiver is then placed at 50 mm intervals around circumference of the pole starting from the transmitter. The receiver is also place at a height 600 mm above the transmitter. The same sets of measurements of done with the transmitter screwed in at a height of 1.2 m from the base of the pole. The measured signals are then taken 600 mm above and below the transmitter level. If all the signals are received correctly then the pole is classified as sound. If they are not received correctly then a full scan of the pole is required. A full scan requires the transmitter to be rotated to three different positions in the same level, from 0^{o} to 120^{o} then 240^{o}. This allows the system to isolate the area in which the signals are attenuated as shown in figure 2.11.

The full scan procedure is done at ground level and repeated at 1m and 2m above ground. The sets of data are then fed into the system for PURL software to analyse. Based on the measurements the software will determine the strength of the pole and if it should be replaced.

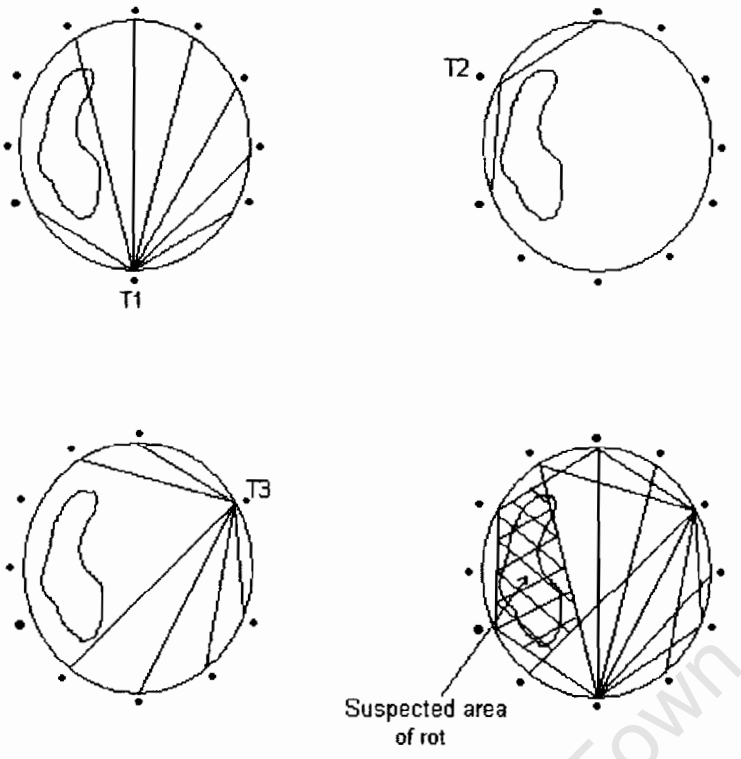

Figure 2.11: Full scan procedure by rotating the transmitter to three position around the pole to detect the area of decay. [18]

2.1.8 PICUS Sonic Tomograph

The PICUS Sonic Tomograph is manufactured by Argus Electronic gmbh [13]. The system is designed to take non-invasive measurements of trees for inspection of wood rot or damage. The system uses the method of sound and time of flight measurements to produce its tomograph. It consists of 10-12 sensors evenly spaced around the tree as shown is figure 2.12. Each sensor is connected to a nail that is driven into the tree. The measurements are taken by tapping the tree with a hammer at each sensor causing a sound wave to propagate through the tree. This then measures the time of flight of the sound wave from the tapped sensor to the adjacent sensors of the tree. The system works on the principle that sound travels faster through wood(solid) than through rot(air). An illustration of the time of flight theory used by the system can be seen in figure 2.13. Here we can see sound waves travelling near the path of the rot or void has to take a longer route to reach the sensors on the other end of the tree.

A series of measurements are produced by the process, storing the time of flight data for the various combinations of sensors. This information is then fed into a Pocket PC which produces false coloured tomographs. An example of such a tomograph is shown in figure 2.14. We can see the damage to the pole quite accurately in the produced tomograph as the purple and blue areas.

You can also take multiple measurements at different heights in order to identify the root

Figure 2.12: PICUS Sonic Tomograph sensors evenly attached to a tree. [13]

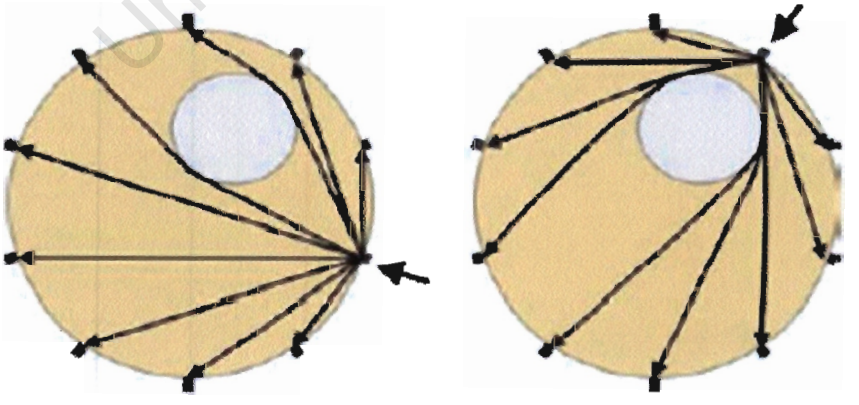

Figure 2.13: Sound propagation through a tree by the tapping of one sensor with a hammer. [13]

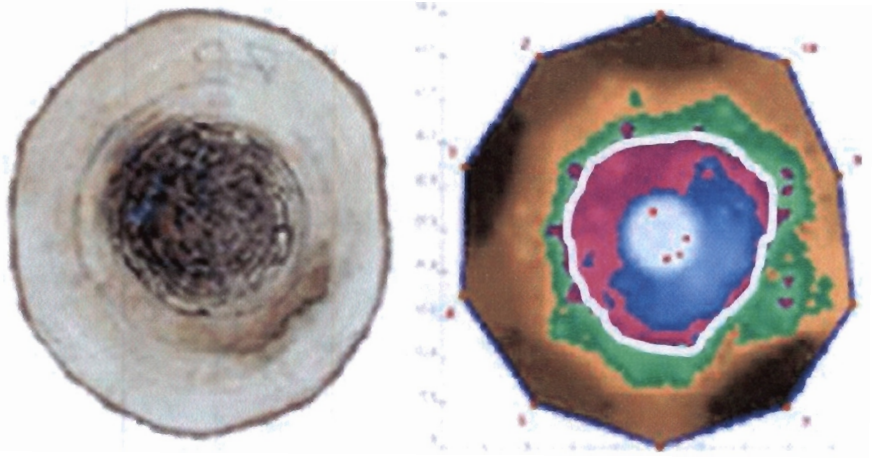

Figure 2.14: A spruce with Heterobasidion annosum and ant damage. The image on the left is the actual tree and the image on the right is a PICUS produced tomograph. [13]

of the decay. One of the limitations of the systems is its inability to distinguish some shapes of cracks in trees from decay. We can see the false tomograph by looking at figure 2.15. Due to the shape of the crack the image produced gives us a false sense of the size of the decayed area. The PICUS system is also limited in that it only produces a tomograph of the tree but it is not a direct test of the strength of the tree. This is left to the inspector to interpret the tomograph and deduce if the tree is healthy or not.

2.1.9 FAKOPP 2D

FAKOPP 2D is produced by a Hungarian company called FAKOPP Enterprises [21]. The system is almost identical in operation to the PICUS Sonic Tomograph system. They are both produced for the purpose of tree evaluation. The system operates on 6-8 sensors using the time of flight method to produce an in situ tomograph on a Palmtop PC. The method for taking the measurements mimics that of the PICUS system in that a hammer is used to generate a stress wave inside the tree. A typical image produced by the system is shown in figure 2.16. The blockiness of the tomograph depicts an accurate reconstruction of the measured data. The PICUS system probably using a smoothing algorithm to produce a its images with more continuity.

2.1.10 Sylvatest

Sylvatest [23] is produced by a Swiss company Sandes SA. The system was designed for grading timber. The system measures ultrasonic wave velocity to determine the state of the timber. It can also be used for wooden pole inspection. The Sylvatest consist of two peizoelectronic transducers, one for transmitting a 30kHz signal into the the wood and the other for receiving the transmitted signal. We can see the setup of the transducers in

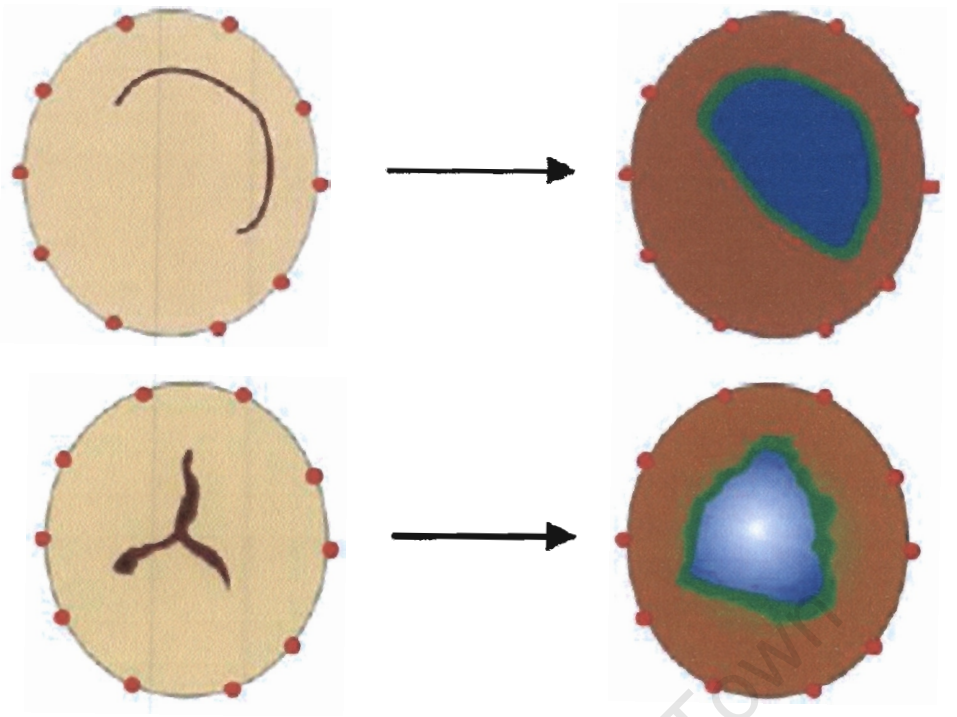

Figure 2.15: Resulting tomographs of crescent and star shaped cracks. [13]

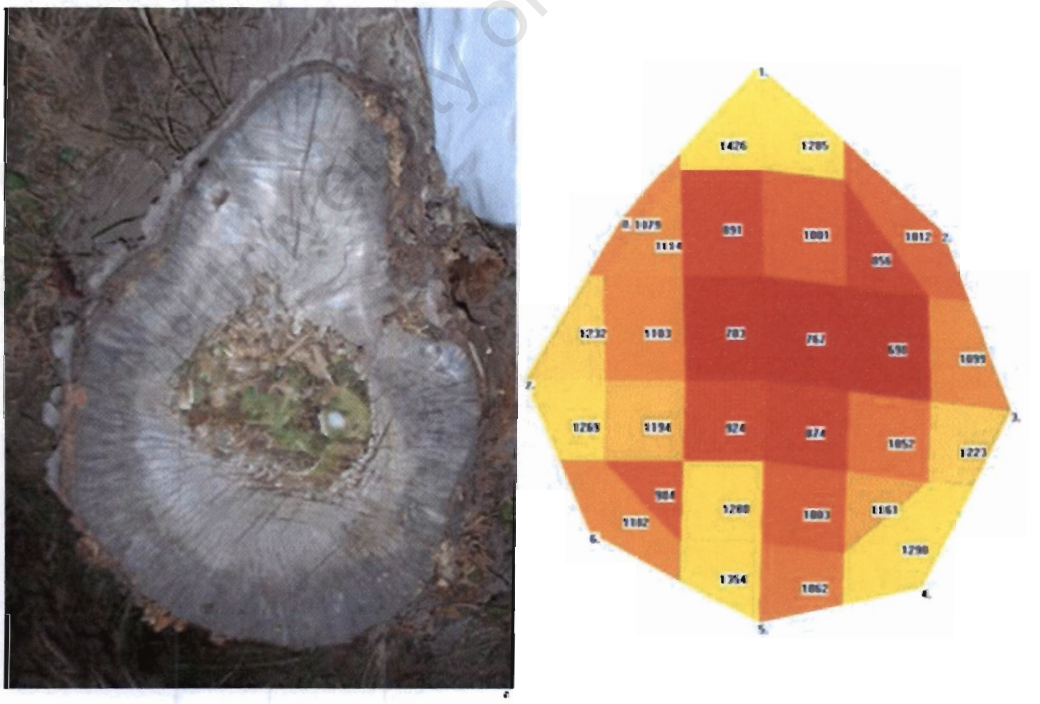

Figure 2.16: Image of a decayed tree(left) with the resulting FAKOPP 2D tomograph(right). [21]

figure 2.17.

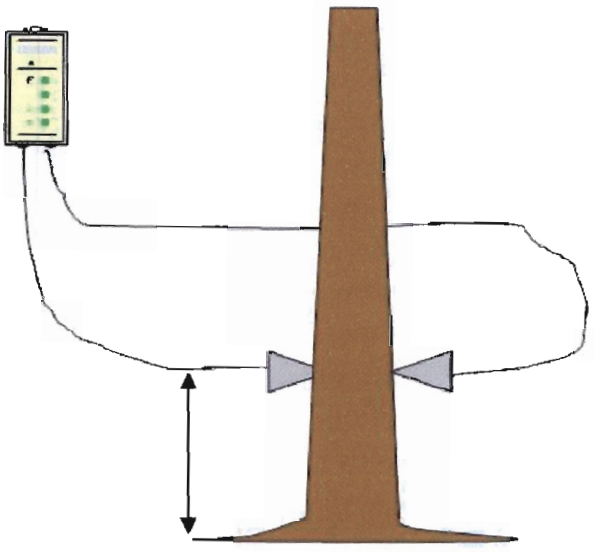

Figure 2.17: Sylvatest setup for tree evaluation [23]

In order to transmit and receive the signals a hole or 5mm diameter has to be drilled to a depth of 1cm to ensure proper coupling of the signal into and from the wood. The receiving transducer is triggered once the transmitted pulse is received. The time taken between the transmission and the reception of the pulse is used to calculate the wave velocity.

The system does not take into account factors such as wood type, moisture content or temperature effects to determine the trees state. This would imply that the system would have to be calibrated with a healthy pole in the same environment as the pole being tested. The system is also invasive as 1cm holes needs to be drilled in the wood.

2.2 Electrical Capacitance Tomography [31]

Electrical Capacitance Tomography (ECT) [31] has been developed mainly for the use of process tomography. It is a relatively fast and low cost method for imaging industrial processes. A typical ECT system would consist of three major components, the sensors (electrodes), the sensing electronics and a computer as shown in figure 2.18. The electrodes are placed around the desired device under test being either a process or medium you want to image. The sensing electrodes in conjunction with the sensing circuitry are used to measure all possible combinations of the capacitance measurements between the electrodes. The computer will read in the measured data and store it. The sensing electrodes as I will discuss later are the most crucial of all these components. This is due to

fact that it would be used to measure the smallest change in the capacitance, which lie within the range of Femto Farads ($10^{-15}F$). Together these components would capture the data from the process in order to reproduce a tomographic image.

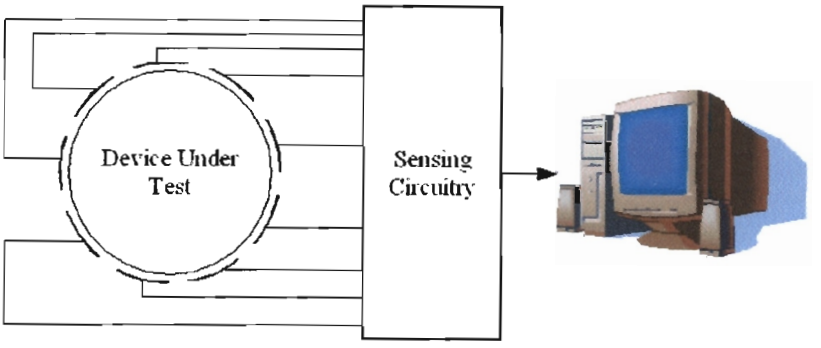

Figure 2.18: ECT components

Due to the fact that the capacitance we are trying to measure is so small it makes it impossible to use normal capacitance transducers, such as laboratory capactiance measuring devices. The capacitance measuring system, beside having to be very sensitive, also has to deal with the issue of stray capacitance. The three main sources of these stray capacitances can be attributed to [31]:

- The shielded cable used for connecting the electrode to the measuring circuit.
- The CMOS switches used to switch between excitation and detection electrodes.
- The shielded housing guarding the electrodes from external noise.

There are two methods in which capacitance tomography progressed due to their ability to be stray immune. These methods can be separated into [31]:

- The charge and discharge method
- The AC based method.

In the following section I will give an overview of the methods of operation, the equations involved in the processes and their downfalls and limitations.

2.2.1 The Charge and Discharge Method [31]

The circuit configuration of the charge and discharge method is shown in figure 2.19. We can distinguish this method into two phases namely the charge and discharge phase. In the charging phase switches S1 and S4 are closed while S2 and S3 are open. During the charge phase we have the charge current flowing from the voltage source through switch S1 and C_x (our device under test) and into op-amp 1. This charge current flowing through the capacitor can be modeled as[31]:

$$Q_1 = V_c C_x$$

From this we can calculate the current I for a particular switching frequency f to be $I_1 = fQ_1 = fV_cC_x$. Op-amp 1 then converts this current into a voltage giving us:

$$V_1 = -I_1R_f = -fV_cC_xR_f + e_1$$

Where e_1 is the DC offset of the op-amp. Similarly we can calculate the discharge phase equation knowing that when switches 2 and 3 are close and 1 and 4 are open the charged up capacitor C_x will discharge through the left to ground. The capacitor $C_x$will then draw its current from op-amp 2 yielding the following equation:

$$V_2 = fV_cC_xR_f + e_2$$

where e_2 is the DC offset voltage of op-amp 2. The signals for the charge and discharge phases are then inserted into a differential amplifier giving us:

$$V_3 = K(V_2 - V_1) = 2KfV_cC_xR_f + K(e_2 - e_1) \tag{2.1}$$

where K is the gain of the differential amplifier. The DC offsets of the op-amps e_1 and e_2 seems to cancel each other out, but this depends on whether the offset values are positive or negative. Seeing that we know all the variables we can now calculate the measured capacitance,C_x. From the above equation we can see that the system is dependant on the frequency of the switching. The higher the switching the stronger the output. The switching is however limited by the rating of the CMOS switches used.

Referring to figure 2.19 we can see that the stray capacitance has been labeled as C_{s1} and C_{s2}. The stray capacitance C_{s1} gets driven straight from the voltage source in the charge phase and gets discharged to ground in the discharge phase. Hence it does not produce any current flow through C_x. The stray capacitance C_{s2} is held at virtual earth by the inputs of op-amps 1 and 2 and therefore has a zero potential across it. We can therefore see that the charge and discharge method is stray immune.

Looking at figure 2.19 we can see that the DC input voltage is modulated by S1 and S4 into a square wave and is demodulated by S2 and S3. The capacitor C between the input pins of the op-amp serve as a low pass filter to the measured signals. Due to the demodulation occurring before the signal amplification, the system is only capable of measuring impedance.

This method does however suffer from a charge injection problem. A typical CMOS switch has a switch coupling capacitance of about 0.5pF whereas we are trying to measure capacitance in the femto Farad range. The differential input does however relieve the charge injection problem slightly but not enough to accurately measure the required data.

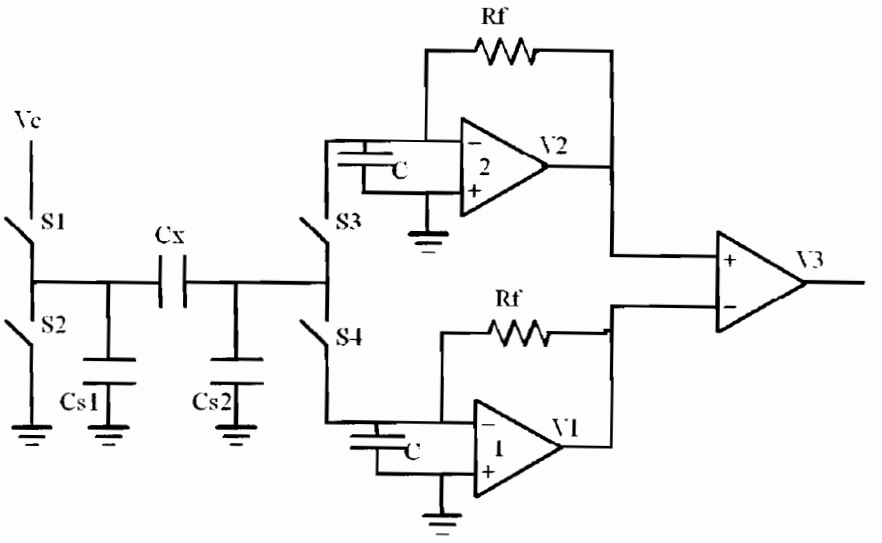

Figure 2.19: Charge and discharge based capacitance measuring circuit

2.2.2 AC-based Method [31]

Unlike the the charge and discharge circuit which uses a switched DC voltage to drive the capacitor, the AC-based method uses a sinusoidal voltage. The circuit configuration for the ac-based method can be seen in figure 2.20.

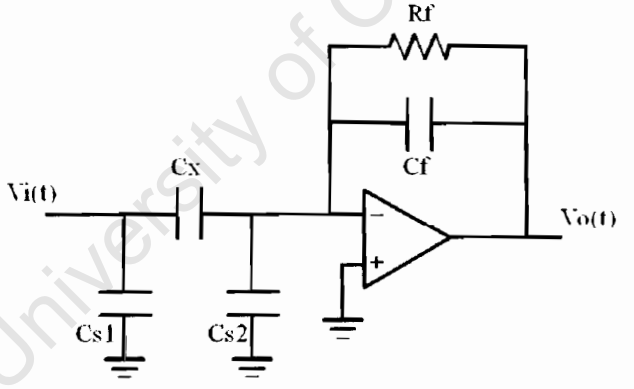

Figure 2.20: AC-Based capacitance measuring circuit

In this configuration we use a single op-amp in feedback configuration to measure the reactance of the capacitor. The feedback resistor is necessary in order to prevent the output of the op-amp drifting to saturation. Ignoring the stray capacitance we can write the equation for the output voltage as the ratio of impedances to be:

$$V_o = \frac{Z_f}{Z_x} V_i$$

thus

$$V_o = \frac{j\omega C_x R_f}{j\omega C_f R_f + 1} V_i \tag{2.2}$$

If we choose a large feedback resistor and a high input voltage frequency then $\mid j\omega C_f R_f \mid \gg 1$ and we can simplify the original equation to:

$$V_o = \frac{C_x}{C_f} V_i \tag{2.3}$$

This equation would then make the output voltage directly proportional to the capacitor C_x and the input voltage and the indirectly proportional to the feedback capacitor. So the smaller the feedback capacitor or the larger the input voltage will give a larger measured signal.

As in the case in charge and discharge method the input stray capacitance C_{s1} is driven directly by the input sinusoidal voltage not producing any charge flow in the direction of C_x and therefore not effecting the measured capacitance. C_{s2} is held in at virtual ground of the input pin of the op-amp and therefore has zero potential across it, making the system stray immune.

The limitations of the AC-based method is that it requires the system to operate at a relatively high frequency, typically between $100kHz$ to $500kHz$, in order to make the measurements phase independent of the component values (the circuit equation simplification, if $\mid j\omega C_f R_f \mid \gg 1$ holds true). The system uses AC amplifiers to boost the measured signal and op-amps capable of operating at high frequencies (hundreds of kHz) are generally quite expensive. The system does not however suffer from charge injection making the system capable of detecting smaller capacitance changes than the charge and discharge method. Due to the fact that the measured signal is still in its AC form after amplification we can use phase synchronous detection to measure either the real or imaginary components.

Chapter 3

EIT System Design

A capacitor's value it partly determined by the dielectric constant of the medium between its electrodes. In a similar manner most objects have a certain permittivity. This permittivity describes how an electric field affects and is affected by the medium. By capturing the impedance value of the object we can analyze the object's permittivity. Most objects have a fixed permittivity and due to this known fact we are able to distinguish objects from one another using impedance tomography. The medium we are interested in testing is wood. Wood does not have a fixed permittivity due to its pourous nature. It is a combination of air gaps and solid material and sometimes water, depending on its moisture content.

As discussed in the literature survey there are two methods of producing a capacitance measuring device for ECT. Due to the nature of the medium that we are imaging we need to take impedance measurements while still being able to distinguish between the real and imaginary components. For this we had to choose the ac-based capacitance system. In the charge and discharge method the phase synchronous detection happens while taking the measurements and before any signal amplification. Due to the location of the phase synchronous detector within the system, the system produces a single signal for analysis which cannot be split into a real and imaginary component. In the ac-based method the phase synchronous detection happens after the signal has been measured and amplified. Due to this the system can be configured by the phase synchronous detector to measure either the real of the imaginary components of the signal. The importance of being able to distinguish between the real and imaginary components of the data gives us the ability to analyse the medium, be it mainly capacitive or resistive.

A basic flow diagram of the ac-based system is shown in figure 3.1. A sinusoidal source signal drives an excitation electrode. This then produces a current flowing in a lead connected to the detection electrode. This current signal is then converted into a voltage by the trans-impedance amplifier and then AC amplified. This AC voltage signal is then passed to the phase synchronous detector which can be configured to output either the inphase or quadrature components of the AC signal. The output of the phase synchronous detector is then passed through a low pass filter (LPF) to produce a DC voltage proportional to the measured capacitance or conductance which is in turn fed in a computer for

analysis. In the coming chapter I will discuss the various aspects we need to take into account for designing and implementing this circuitry.

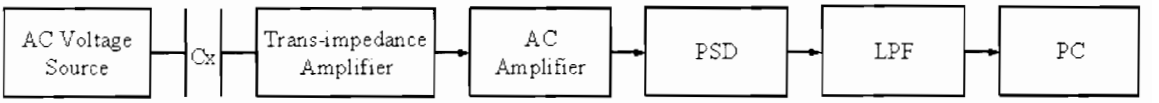

Figure 3.1: Flow Diagram of an ac-based impedance measuring circuit

3.1 Approach

The obvious approach to taking the capacitance measurements would be to drive a signal between a pair of electrodes in order to measure a fixed capacitance value. This would then be repeated for all the combinations of electrode pairs possible. If we had to take an N electrode system it would give us, $\frac{N(N-1)}{2}$ combinations, where N is the number of electrodes. For a 12 electode system this corresponds to 66 combinations to get a complete data set for processing. If the measurement circuitry had an approximate time of say $0.1ms$ per combination, this would include the switching time required by the analog switches, measuring of the signal and settling of the filters, it would take 6.6 seconds to capture a complete set of data. In addition to the slow capturing time of data this approach also requires the electrode select switches need to have an extremely high open circuit impedance in order to isolate the signal transfer from source to receiving electrode.

An alternative approach would be to capture all the data simultaneously while driving only one electrode and measuring on the remaining electrodes simultaneously. The other electrodes would all be virtual earth inputs to trans-impedance amplifiers. In this method we would only need to rotate the driving signal to each of the 12 electrode positions in turn. For this parallel measurement approach it would now only take 12 times the time to abtain a complete set of data instead of 66 times, which makes it 5.5 times faster. This approach wouldn't suffer from the high open impedance problem as all the receiving electrodes are measuring the signal across the device under test. How this works will be explained in the following sections.

3.2 Circuit Design

For the purpose of understanding the measurement system we will take a look at a single functional pair of electrodes. As shown in figure 3.1, the measurement circuit can be split into a chain of four modules:

- trans-impedance amplfier
- AC amplifier
- the phase synchronous detector

- the low pass filter

These components make up the sensing circuitry attached to a single electrode in figure 2.18. The part of the design that controls the measurements, i.e. the multiplexing is not included in this section and will be dealt with in section 3.3.

3.2.1 Trans-impedance Amplifier

As we reviewed in the literature survey the AC-based method is based on the fundamental equation 2.3 that

$$V_o = \frac{C_x}{C_f} V_i$$

if $\mid j\omega C_f R_f \mid \gg 1$. Otherwise equation 2.2 will still hold for the output of the trans-impedance amplifier. It was anticipated however, that the impedance between the two plates may not be purely capacitive and hence a full impedance measurement would be required. Due to this, we need to remodel the circuit in figure 2.20 to include the conductance in the device under test. We now have to model the equivalent device under test as an impedance, Z. The equivalent circuit now modified from figure 2.20 is shown in figure 3.2.

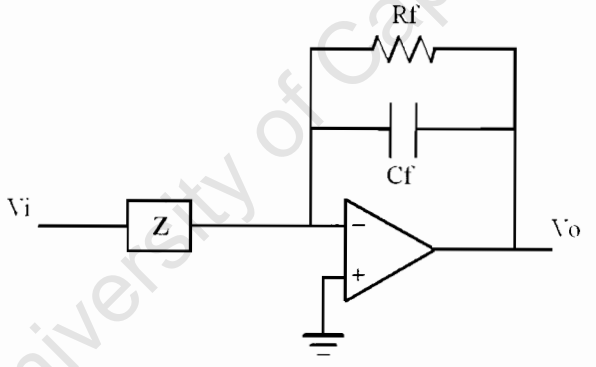

Figure 3.2: AC Based Impedance measuring circuit with trans-impedance amplifier

If we model the feedback impedance as Z_f being the parallel combination of R_f and C_f, the output voltage becomes

$$V_o = \frac{Z_f}{Z} V_i \tag{3.1}$$

If we model the impedance of the device under test as an admittance we can rewrite equation 3.1 as

$$V_o = Y Z_f V_i \tag{3.2}$$

Now if we split the admittance Y into $G + jB$ and clump together the known constants $Z_f V_i = K$ we can simplify the equation to $V_o = (G + jB)K$. Therefore in practice we will be able to calculate the value of the impedance Z (or conductance Y) in the device under test due the fact that we know all the other variables.

Now that we are measuring the full impedance of the device under test let us see what happens to the equations when we make a few assumptions. In terms of $R_f$and C_f, the feedback admittance is

$$Y_f = \frac{1}{R_f} + j\omega C_f = G_f + jB_f \tag{3.3}$$

If $\omega C_f \gg \frac{1}{R_f}$ we can rewrite the admittance Y_f to be only jB_f and if we assume that the device under test is going to be mainly imaginary or capacitive,ie. $jB \gg G$, then we can rewrite equation 3.2 as:

$$\begin{aligned} V_o &= jB.\frac{1}{jB_f}V_i \\ &= \frac{B}{B_f}V_i \end{aligned} \tag{3.4}$$

where B and B_f are actually ωC and ωC_f respectively, giving us the approximate relationship

$$V_o = \frac{C}{C_f}V_i$$

which ties up with the original AC capacitance tomography equation as shown in equation 2.3, which holds only for a dominately feedback impedance, and a dominately capacitive impedance to be measured.

If we don't assume anything about the device under test we can work out the output equation starting with equation 3.2.

$$\begin{aligned} V_o &= YZ_fV_i \\ &= \frac{(G+jB)}{(G_f+jB_f)}V_i \end{aligned}$$

Working through we get

$$V_o = [(G\frac{G_f}{B_f} + B) + j(B\frac{G_f}{B_f} - G)]\frac{B_f}{G_f^2 + B_f^2}V_i \tag{3.5}$$

where$\frac{B_f}{G_f^2+B_f^2}V_i$ is a constant, K. If we model the feedback impedance as dominately capacitance we get $\omega C_f \gg \frac{1}{R_f}$ which is $B_f \gg G_f$ making $\frac{G_f}{B_f} \to 0$. Now we can rewrite the equation 3.5 as:

$$V_o = (B - jG)K \tag{3.6}$$

Looking at equation 3.6 we can conclude that if the impedance of the device under test is modelled as a parallel resistance and capacitance as shown in figure 3.3 we can deduce that the real part (inphase or "I" channel) would consist of mainly $B \propto C_x$ and the imaginary part (quadrature or "Q" channel) would consist of mainly $G \propto \frac{1}{Rx}$. Where G was initially the real and B was the imaginary part of the admittance.

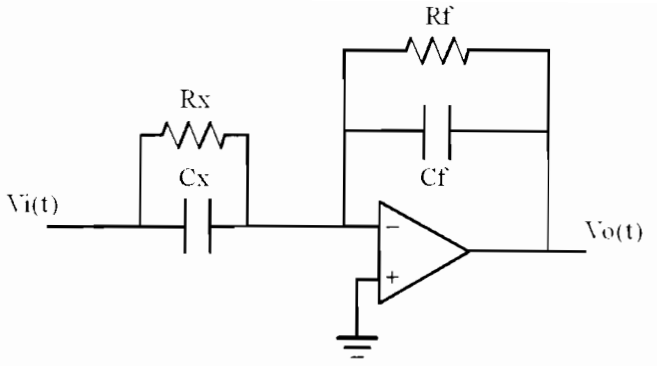

Figure 3.3: AC based method with impedance modelling

In the actual assembly of the the trans-impedance amplifier I used an excitation frequency of $125kHz$ and C_f and R_f of $10pF$ and $2.2M\Omega$ respectively. Using these values to prove that $\omega C_f \gg \frac{1}{R_f}$ does not exactly hold true but give us a good approximation to it. If we substitute in the values of $125kHz$, C_f and R_f we get $\omega C_f = 18$ and $\frac{1}{R_f} = 1$ if simplified. These values were chosen to try and maximise the gain of the measurement as the DUT we are measuring would normally be mainly capacitive. Equation 3.4 would therefore allow us to increase the gain by decreasing the feedback capacitive value.

To put the amplitude of the measurements into perspective we can imagine the DUT to be purely capacitive. If the electrodes used to measure the capacitance were $0.180m$ apart and had a surface area of $30mm \times 100mm = 0.003m^2$ we can very crudely calculate the capacitance in air using the equation $C = \varepsilon\frac{A}{d}$ where $\varepsilon = \varepsilon_o\varepsilon_r$ and ε_o is the permittivity in a vacuum, $8.85 \times 10^{-12}\frac{C^2}{N.m^2}$, and ε_r is the relative permittivity of air, being 1. The resulting capacitance will be $0.15fF$. From this value we can see that it is way below the capacitance component values we deal with in normal electronics. Therefore we need to amplifiy the measured data by as much as possible in order for us to properly measure it.

3.2.2 AC Amplifier

The trans-impedance amplfier converts impedance of the DUT into a measurable voltage. This measured voltage can only be amplified by two means. We can reduce the feedback capacitor, B_f, to the lowest available capacitor with high tolerance, or we can increase the amplitude of the driving signal without saturating the outputs of the op-amps of the detection electrodes adjacent to the driving electrode. The rest of the amplification has to be done by an AC amplifier in order to make the signal usable for phase synchronous detection. The only valid information from the output of the trans-impedance amplifier is the AC signal. Any DC introduced by the measurement is irrelevant as we are injecting AC signals into the drive electrode and measuring the change in phase and amplitude due to the medium. The DC offsets produced by the op-amp need to be nulled. To do this we add a DC blocking capacitor immediately after the trans-impedance amplifier as shown in figure 3.4. In this way when we can amplify the AC signal without the DC offsets which

would otherwise cause the input signal to saturate to the supply rails. For this we use a $10\mu F$ capacitor, which has an AC impedance of 0.127Ω at $125kHz$.

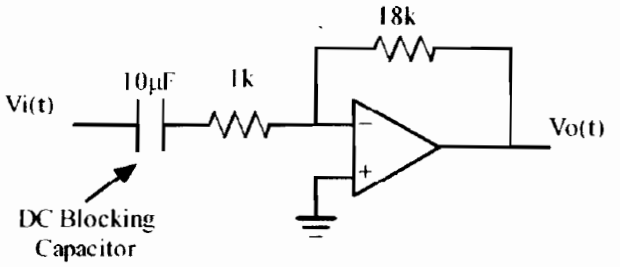

Figure 3.4: AC Amplifier

Now that we have taken out any DC components from the measured signal we can amplify the signal by using a standard inverting amplifier configuration as shown in figure 3.4. A voltage gain of 18 was chosen for this amplfier such that the signal at the output will reach at most about 10 Volts under typical operating conditions, in order not to saturate the signal of the highest measured amplitude. The high pass filter created by the DC blocking capacitor and the input resistor lies at a frequency of $16Hz$ which does not lie close to the operating frequency of $125kHz$.

3.2.3 Phase Synchronous Detector

In order for us to measure the relevant components of the impedance we need to pass the measured and amplified AC signal through a phase synchronous detector. The phase synchronous detector will consist of the measured signal being multiplied by either the input reference signal, I, or a 90^odegree phase shifter version, Q, of this signal as shown in figure 3.5 in order to obtain both the real and imaginary parts of the signal.

If we refer back to equation 3.6 we can look at the value of the constant which consisted of $\frac{B_f}{G_f^2+B_f^2}V_i$ where V_i is the phasor representation of the sinusiodal signal $V_i = Kcos\omega t$, where K is the amplitude. If we look at the system equation 3.6 we can deduce that the output would therefore consist of a sinusoidal waveform with an amplitude and phase shift proportional to the DUT. This can be written as $A\cos(\omega t - \theta)$ or as the phasor $V_o = Ae^{-j\theta}$, where θ is the phase shift caused by the complex measurement $(B - jG)$ as derived from equation 3.6 .

If we take this simplified output and multiply it by the reference waveform to get:

$$\begin{aligned} I(t) &= A\cos(\omega t - \theta)(\cos\omega t) \\ &= \frac{A}{2}[\cos(2\omega t - \theta) + \cos(-\theta)] \\ &= \frac{A}{2}\cos\theta + \frac{A}{2}\cos(2\omega t - \theta) \end{aligned} \tag{3.7}$$

The output after I channel phase synchronous detection contain two parts, a high fre-

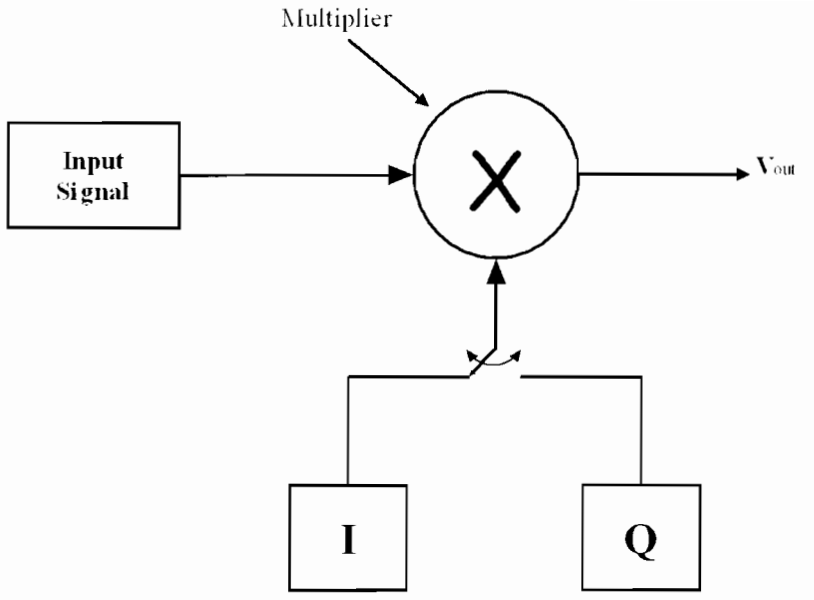

Figure 3.5: Phase Synchronous Detector

quency component and a DC component. In the next section we use a LPF in order to remove the high frequency component leaving us with the DC component which is proportional to the real part of our measurement. We can prove the same for the Q channel. In order to extract the imaginary term with the correct sign as shown in $(B - jG)$ we multiply by a "$-\sin\omega t$" term giving us:

$$\begin{aligned} Q(t) &= A\cos(\omega t - \theta)(-\sin\omega t) \\ &= -\frac{A}{2}[\sin(2\omega t - \theta) - \sin(-\theta)] \\ &= -\frac{A}{2}\sin(\theta) - \frac{A}{2}\sin(2\omega t + \theta) \end{aligned} \tag{3.8}$$

We can now see the imaginary term, $Q(t)$, as negative and the real term, $I(t)$, as positive from the above calculations. If the measured signal from the trans-impedance amplifier has a zero phase shift we would, by substituting $\theta = 0^o$ into equations 3.7 and 3.8, end up with only real term as $\cos 0^o = 1$ and no imaginary term as $\sin 0^o = 0$ for the DC components. The outputs of the phase synchronous detector would look similar to a rectified waveform at double the frequency as shown in figure 3.6.

3.2.4 Low Pass Filter

Now that the signal had been differentiated into a rectified version of its real and imaginary components we can extract the relevant information in order to analyse the measured signal. The primary source of the information would be the amplitude of the measured signal. This is due to the fact that the frequency does not change across any of the measured electrodes. The phase may vary due to the nature of the medium and will increase or decrease the amplitude of the in-phase or quadrature components. The resulting DC

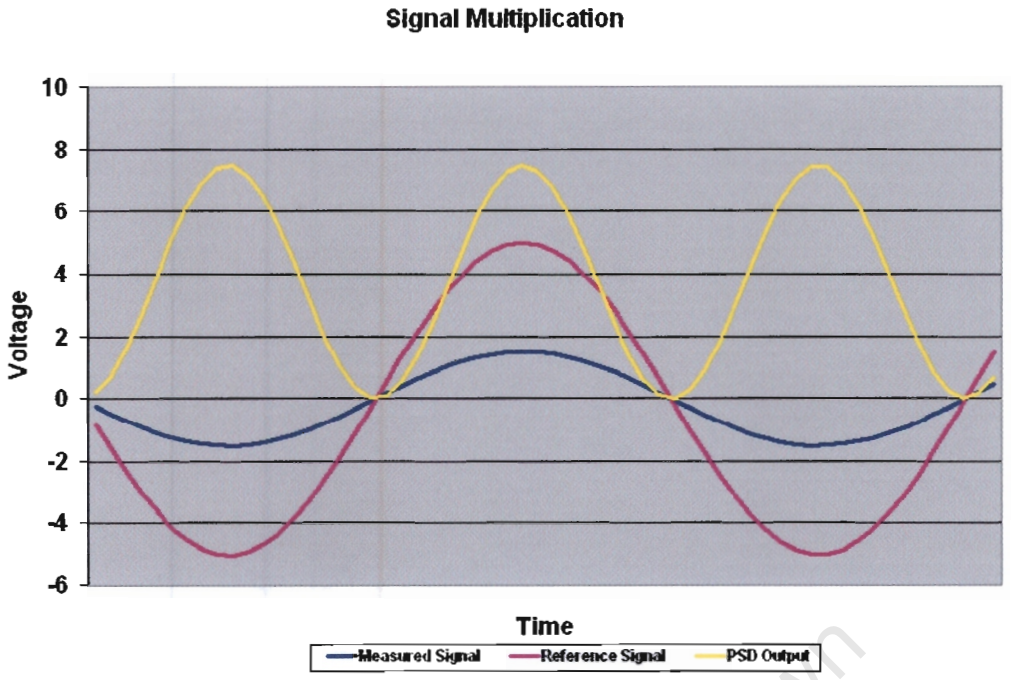

Figure 3.6: Signal Multiplication in the phase synchronous detector

amplitude is proportional to the amplitude of the measured signal. In order for us to extract this information we pass the signal through a low pass filter. The LPF eliminates the unwanted 2ω frequency component as well as reducing the bandwidth and hence the noise. In order to capture the data at a high rate into the DAQ we need a fast acting filter with a quick settling time. The LPF we used is a standard RC LPF where $R_f C_f$ is connected as the feedback components of an op-amp as shown in figure 3.7.

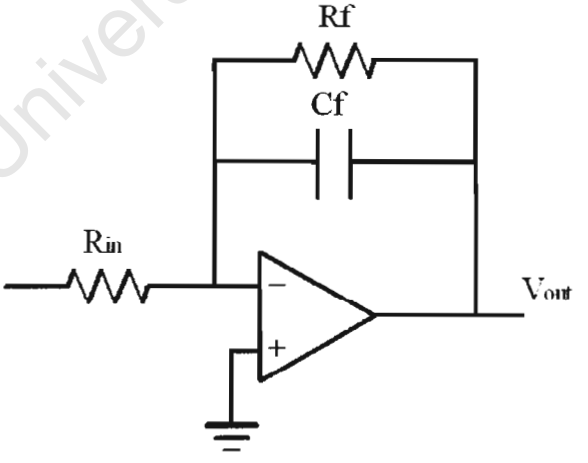

Figure 3.7: Low Pass Filter

The equation governing the cut off frequency of a LPF is $f = \frac{1}{2\pi RC}$ where RC are the values of the feedback components. Using the values of $R_f = 100k\Omega$ and $C_f = 10nF$ we get a cut off frequency of $160Hz$. The time constant of such a configuration is $\tau = RC =$

$0.001sec$. So in order for us to be able to measure the DC component of the signal we would need to wait until the filter settles to about 99% of its final value which is calculated by $V_{out} = V_{in}(1 - e^{-\frac{t}{RC}})$. If we decide to wait 8 time constants, $0.008sec$, we will get a final value that is $(1 - e^{-\frac{t}{RC}}) \times 100 = 99.9\%$ of the settled signal.

The LPF is the final stage of the analog signal processing. The measurable DC signal from the LPF is directly proportional to the the amplitude of the signal captured from the detection electrode which is relatively proportional to the permittivity of the medium through which the driving signal had to travel. This signal is then passed onto the data capturing device which will be discussed in the next section. A complete overview of the analog signal processing can be seen in figure 3.8 which can be directly linked to the flow diagram of figure 3.1.

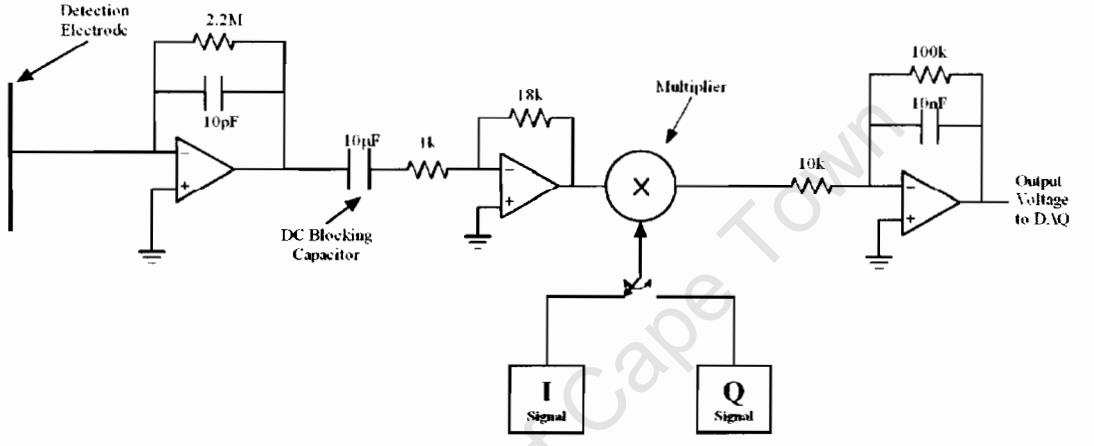

Figure 3.8: Overview of the measurement circuitry for one electrode.

3.3 Multiplexing and Control

The entire system needs to be able to take impedance measurement on a number of different electrode combinations. This section will deal with the circuitry used to switch between a driving electrode and a detection/measurement electrode. It will also deal with the switching between the I and Q channel for phase synchronous detection and the method by which all of this is controlled.

The system will consist of a number of electrodes and as previously explained, each electrode will be given the task to either drive the signal against the medium or detect the driven signal through the medium. So at any one time in a measurement set we will have, in an N electrode system, $N(N-1)$ possible measurements. In a 12 electrode system we would need to take 132 measurements. In order to speed up the process we decided to measure all the readings from the detection electrodes in parallel as explained in section 3.1. So instead of waiting for 132 measurements we can get all the information in the time it takes to take 12 measurements.

3.3.1 Multiplexing and Switching

The actual multiplexing is done with a set of switches that are controlled via a selectable decoder. The decoder receives a signal from the PC telling it which electrode to activate as the driving electrode. The decoder then sends a signal to the relevant switches which in-turn switch the electrode to driving signal. We can see this configuration in figure 3.9. The system is configured so that the decoder can only select one electrode to drive at a time. Therefore when the one electrode is driving all the rest remain in detection mode, ie. connected to the measurement circuitry.

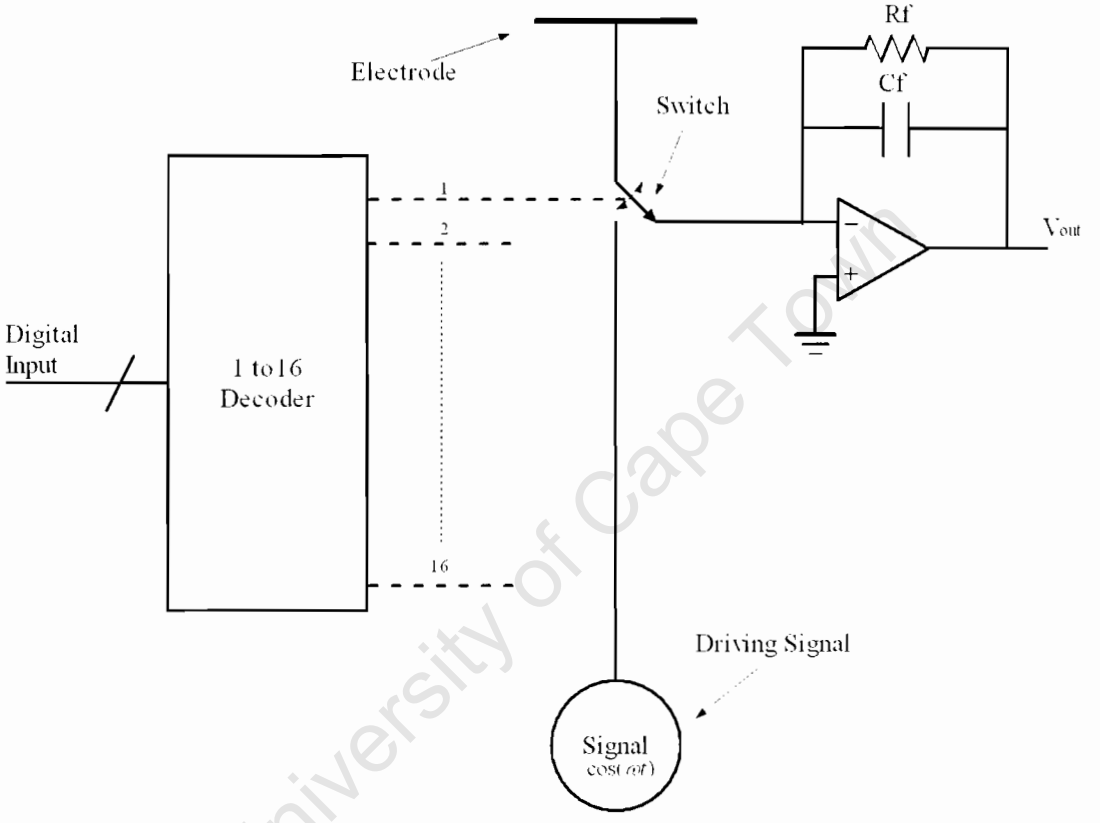

Figure 3.9: Decoder Selecting between drive and detection electrode

The switch used for selecting the drive electrode is not as simple as figure 3.9 depicts. Due to the very small signals we are measuring any sort of coupling between the gap of the switch and the driving signal would drown out the actual measurement. Due to this factor we needed to implement a high isolation T-switch instead of a normal two way switch. A T-switch consists of three switches where the one switch works in anti-phase with the other two. A diagram of a T-switch is shown in figure 3.10. When S1 and S2 are open, S3 is closed. In the configuration we can see that if any of the driving signal is coupled over the gap of S1, it will be forced to ground via switch three. This arrangement gives us a greater off resistance and isolation compared to a normal two way switch. When we want to select the electrode to drive, switch one and two will close and switch three will open allowing the driving signal to flow through to the electrode. At the same time the switch which connects the electrode to the measurement circuitry will open isolating the driving

electrode from its measurement circuitry (being a virtual earth).

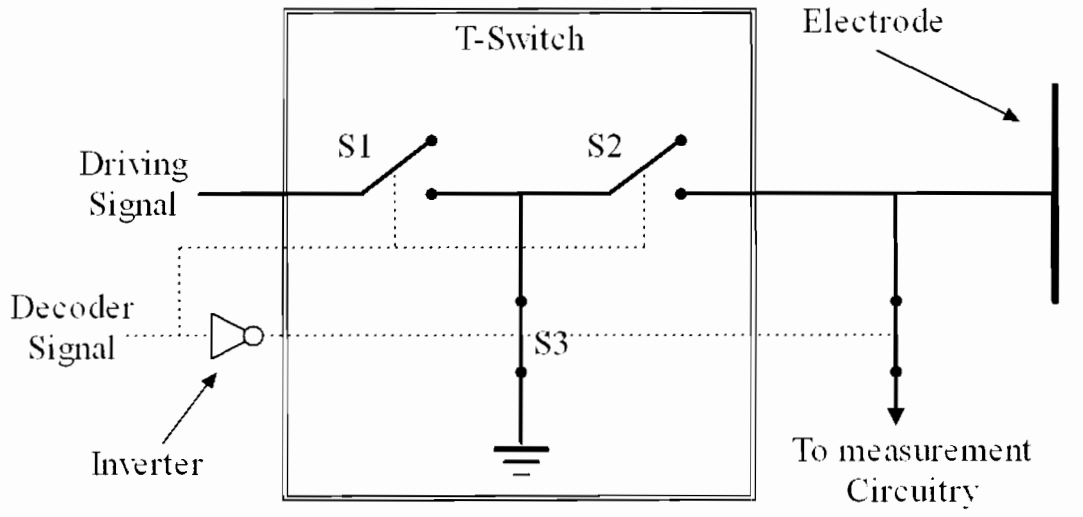

Figure 3.10: T-Switch

The phase synchronous detector requires the switching in of two signals, in-phase and quadrature to the driving electrode. These signals are controlled by a switch which is controlled by the data aquisition card (DAQ). The DAQ tells the switch which signal to pass on to the measurement circuitry. The signal that is supplied through the switch is directed to all the multipliers on every measurement channel. Once the measurements have been taken with the in-phase signal the quadrature signal is switched in. The switching in of the I and Q channels can be seen in figure 3.11.

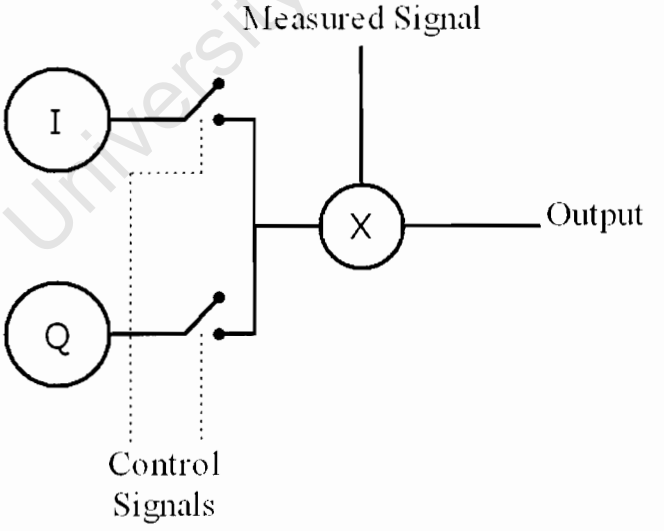

Figure 3.11: Phase synchronous I and Q switching

3.3.2 Data Acquisition Card

The DAQ controls all the switching involved with controlling the system. It is also responsible for generating the signals required to drive and demodulate the system as well

as recording the measured data. The DAQ used for the testing of the system was a National Instruments PCI DAQ card, model number PCI-MIO-16-E. It consisted of:

- 16 analog input
- 2 analog outputs
- 6 digital outputs
- a $1.2MHz$ input sampling rate
- a $1MHz$ output clock rate on the digital to analog converter (DAC)

All the outputs of the measurement channels were connected to the analog inputs of the DAQ. Thus all the measured data was read straight into the PC via the DAQ. Since the signal that was read into the DAQ was a DC signal we did not need a high sampling rate at the DAQ's input channels. Thus the card was more than adequate to measure all the data.

The in-phase, driving and quadrature signals that were required for phase synchronous detection and the driving electrode were generated by the DAQ. The DAQ was used to produce a stepped approximation to a sinusoidal signal of $125kHz$. The $1MHz$ output clock allowed a stepped sinusoidal figure with 8 samples. Hence we got the frequency of $125kHz = \frac{1MHz}{8}$. We needed an even number of samples in order to recreate the quadrature equivalent of the same sinusoidal signal. By shifting the samples of the original signal by a quarter of a period, ie. two samples to the left, a perfectly shifted 90^o signal which is equivalent to $-\sin(t)$ is obtained. We can see the output samples in figure 3.12. These are the samples that are fed into the DAC.

The signals shown in figure 3.12 are not well suited for driving our circuit. They contained all the information needed to generate a pure sinusoidal signal but we needed to filter the signal in order to produce it. We used a simple LC bandpass filter in order to produce a smoothed out version of the stepped signal, allowing only the $125kHz$ component of the signal to pass. The configuration of the LC filter can be seen in figure 3.13.

Using the values of $L = 2.28mH$ and $C = 0.7nF$ we obtained a frequency of :

$$\begin{aligned} f &= \frac{1}{2\pi\sqrt{LC}} \\ &= 126kHz \end{aligned}$$

The DAQ also has 8 digital control lines. These digital lines were used to operate the switching. The decoder required a binary number in order to select the driving electrode. Four digital lines were used in order to operate the decoder enabling one to choose any one of the sixteen outputs. An additional digital line was used to the decoder to control

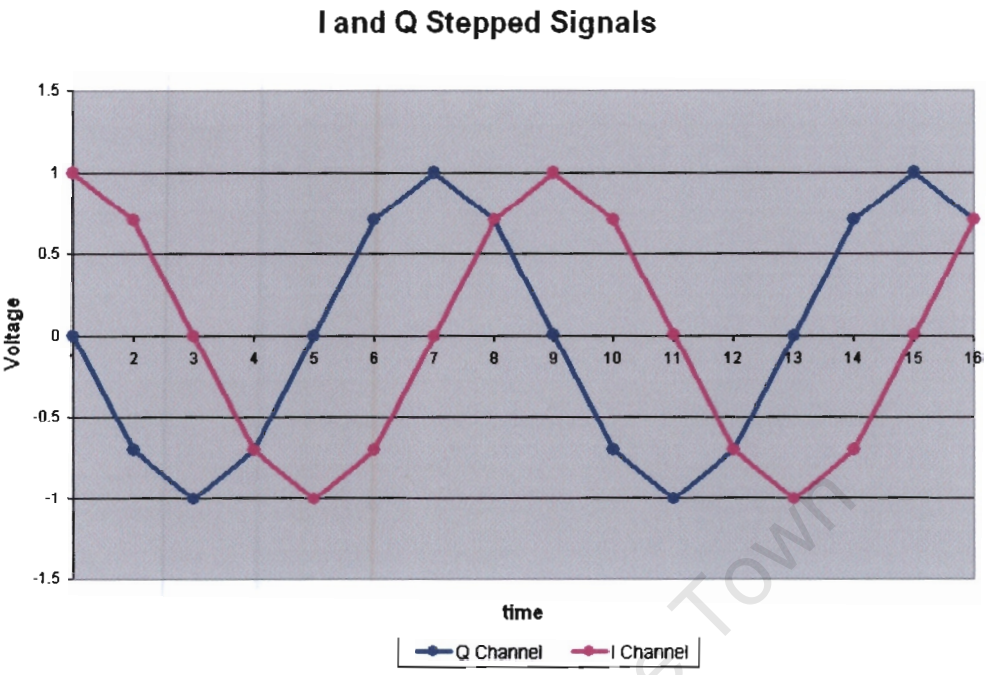

Figure 3.12: Stepped output signal generated by the DAQ

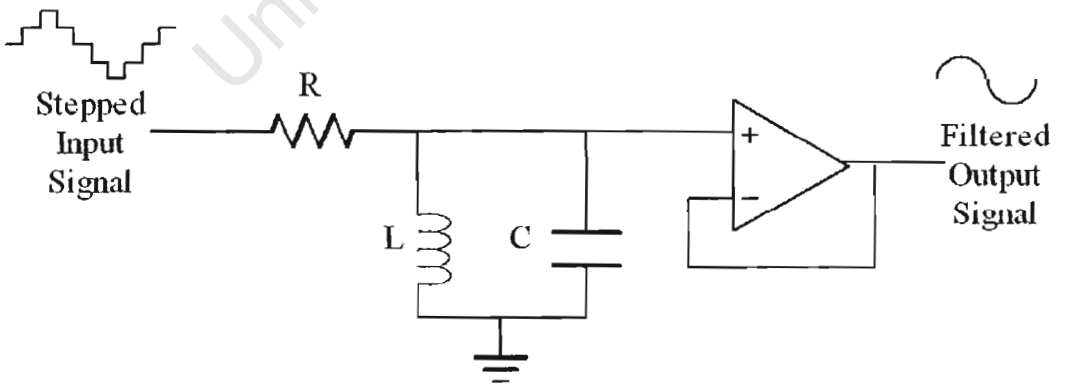

Figure 3.13: *LC* filter used to reproduce perfect signals

the inhibit pin. This allowed us to be able to measure the DC offsets on all the channels while driving on none of them. This was needed in order to calibrate the system and for debugging purposes. Now five of the digital lines have been used just to select the driving electrode. Two more lines are used to switch between the I and Q channels for demodulation.

So from the DAQ we control the entire circuit, ie. the DAQ is used to:

- record all the measured data via the analog inputs
- generate the I and Q signals via the analog outputs
- control the selection of the driving electrode as well as the I and Q demodulation switching via the digital control lines.

A block diagram of the entire switching system including the flow of the measured signal can be seen in figure 3.14. From the figure we can see the switching in of the I and Q channels via the digitals lines, $D5$ and $D6$. We can also see how D and $D_{anti-phase}$ switch the T-switches in order to either drive or detect the signal. Two T-switches are used, as shown by the dotted outlines, in order to further prevent any of the driving signal coupling into the measured signal. The two T-switch configuration helped due to the fact that the isolation switching was done in two stages on two separate chips preventing any coupling occurring within a chip. On the second T-switch we use the fourth switch included inside the chip to control the isolation of the measurement circuitry. We have two LC filters, one for filtering the drive signal and one for filtering the phase synchronous detection signals. Both LC filters have matching components in order to give them identical characteristics. The drive signal as we can see is derived from the same source as the phase synchronous detection I reference signal. The bulk of the circuitry is combined in the blocks labelled, "Trans-impedance Amp", "X" and the "LPF."

3.4 Component Considerations

In this section I will review the components that were used to assemble the circuitry and the requirements and reasoning behind them.

3.4.1 Trans-impedance Amplifier and AC Amplifier

The operating frequency of $125kHz$ required a fast operational amplifier. The op-amp also needed to have low noise. The op-amp choosen was a National Semiconductor high speed operational amplifier, $LM6364$[24]. This op-amp has a gain bandwidth product (GBP) at a frequency of $175MHz$ which is more than 100 times the frequency we are working at. It runs off a wide supply range of ± 36 volts, leaving us with sufficient play in order to accommodate the other components. Due to the small scale of the measurements

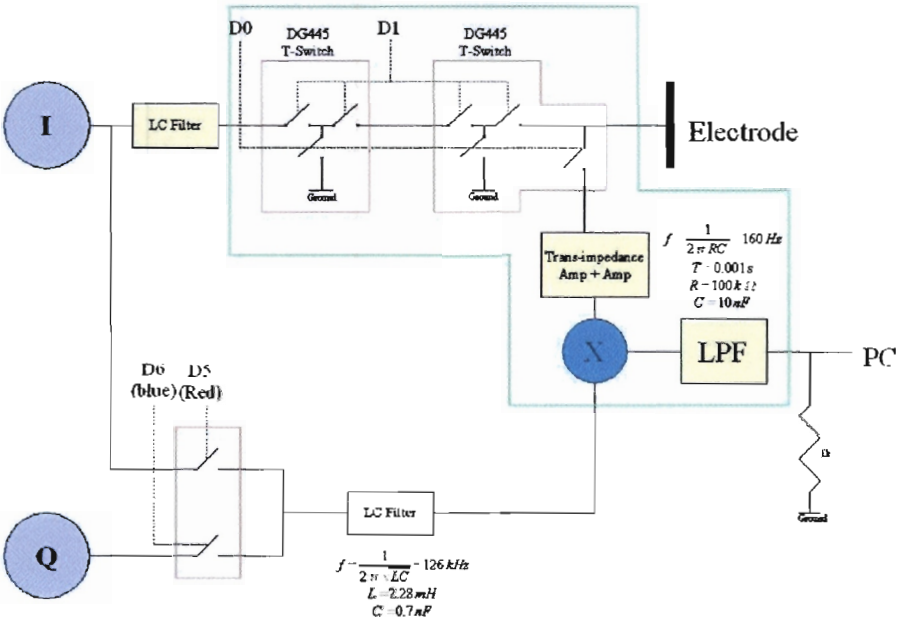

Figure 3.14: Overview of entire switching system

the noise performance of the opamp was investigated. The input voltage noise for the opamp is calculated from[15]

$$e_A^2 = e_n^2 + R_1^2 i_n^2 \tag{3.9}$$

where e_A is the input voltage noise generated by the opamp and e_n and i_n is the input noise voltage and current as found in the datasheet of the opamp. The model used for equation 3.9 is shown in figure 3.15.

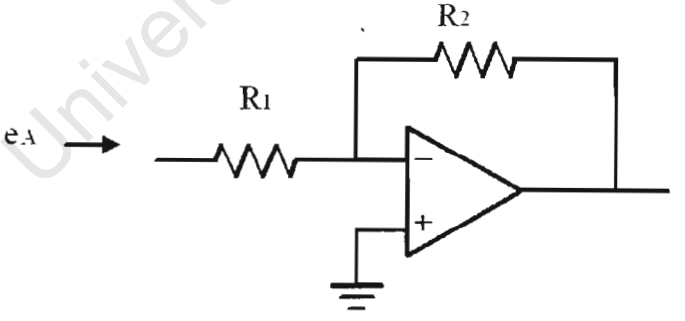

Figure 3.15: Model used for input noise voltage equation

The data sheet specification for the noise voltage is $e_n = 8\frac{nV}{\sqrt{Hz}}$ and the noise current is $i_n = 1.5\frac{pA}{\sqrt{Hz}}$ for this particular op-amp. We are only concerned with the noise that is translated in the final stage of the system. If our bandwidth for the final stage is $100Hz$ we will have:

$$e_n^2 = (8\frac{nV}{\sqrt{Hz}})^2 \times Bandwidth$$

$$= (8\frac{nV}{\sqrt{Hz}})^2(100Hz)$$
$$= 6.4 \times 10^{-15}V^2$$

and:

$$i_n^2 = (1.5\frac{pA}{\sqrt{Hz}}) \times Bandwidth$$
$$= 2.3 \times 10^{-22}A^2$$

The limited input noise voltage and current bandwidth can be illustrated in the figure 3.16.

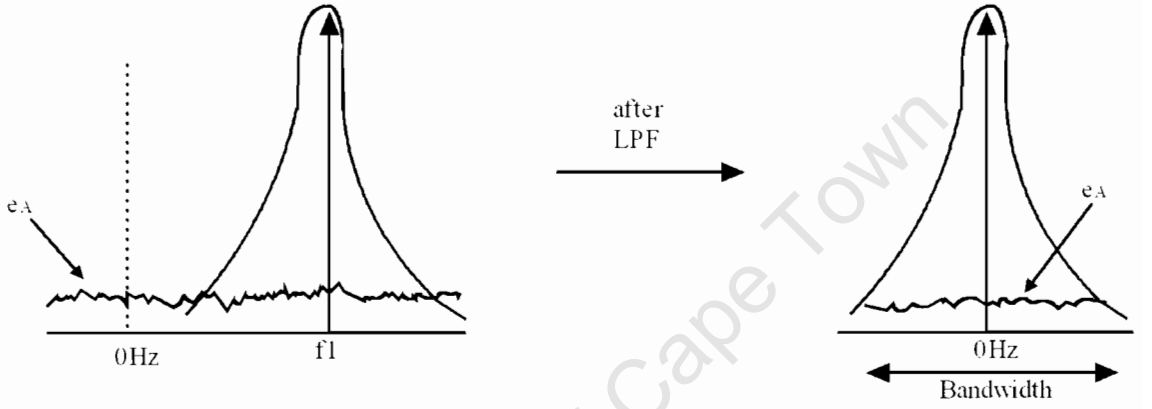

Figure 3.16: Input voltage noise bandwidth

Using the equation for input noise voltage we can calculate the noise generated by each stage of the circuitry. In the first stage, trans-impedance amplifier, we assume that the impedance as shown in figure 3.2 is a pure capacitor of value $50fF$ which is more than likely the case in a dry wooden pole. Using this assumption we calculate the impedance seen by the input of the op-amp as:

$$X_1 = \frac{1}{\omega C} = 23M\Omega$$

using the frequency of $125kHz$.

By substituting this impedance and the e_n and i_n values we calculated into equation 3.9 we get:

$$e_A^2 = e_n^2 + X_1^2 i_n^2$$
$$= 6.4 \times 10^{-15}V^2 + (23M)^2(2.3 \times 10^{-22}A^2)$$
$$= 6.4 \times 10^{-15} + 1.2 \times 10^{-7}$$
$$= 1.2 \times 10^{-7}V^2$$

making the first stage input noise RMS voltage:

$$e_{A1} = 0.35mV\,(RMS)$$

(

In the calculation note how the second term dominates due to the high input impedance. In this section we can deduce that the circuit is current noise sensitive. For the second stage as shown in figure 3.4 we have a capacitor and resistor and the input impedance. Their equivalent impedance is:

$$\begin{aligned} X_2 &= \frac{1}{\omega C} + R \\ &= 1.3 + 1k \\ &\approx 1k\Omega \end{aligned}$$

Substituting this into equation 3.9 as before we get:

$$\begin{aligned} e_A^2 &= 6.4 \times 10^{-15}V^2 + (1000)^2(2.3 \times 10^{-22}A^2) \\ &= 6.6 \times 10^{-15}V^2 \end{aligned}$$

Thus in the second opamp stage, the voltage noise in the opamp dominates. Leaving us with a second stage input noise RMS voltage of:

$$e_{A2} = 81nV\,(RMS)$$

Now we take a look at our actual input signal amplification assuming that equation 2.3 holds for a true capacitance DUT. If we drive the electrode with a signal of amplitude $5V$ the output of the first stage will be:

$$\begin{aligned} V_{out} &= \frac{C_{DUT}}{C_f} V_{in} \\ &= \left(\frac{50 \times 10^{-15}}{10^{-11}} \right) \times 5 \\ &= 5 \times 10^{-3} \times 5 \\ &= 25mV \end{aligned}$$

The RMS output voltage for the 1st stage opamp is

$$V_{out} = \sqrt{2} \times g \times V_{in}\,Volts\,(RMS)$$

where g is the opamp gain, $\frac{C_x}{C_f}$. The output voltage noise for the 1st stage is

$$V_{noise\,out} = g \times e_A\, Volts\,(RMS)$$

where $e_{A1}$is the calculated input voltage noise, $0.35mV$. The ratio of the noise voltage over the output voltage yields the percentage noise in the output of the opamp

$$\begin{aligned} \frac{V_{noise\,out}}{V_{out}} \times 100 &= \frac{g \times e_{A1}}{\sqrt{2} \times g \times V_{in}} \times 100 \\ &= \frac{e_A}{\sqrt{2} \times 5} \times 100 \\ &= \frac{0.35 \times 10^{-3}}{7.07} \times 100 \\ &= 5 \times 10^{-3} \end{aligned} \tag{3.10}$$

Therefore the percentage noise added on the1st stage is $5 \times 10^{-3}\%$ of the actual output voltage.

Using the calculated voltage output of the 1st stage, $25mV$, for input of the 2nd stage and the input noise voltage of $e_{A2} = 81nV$ we get a percentage noise using equation 3.10 of

$$\begin{aligned} \frac{V_{noise\,out}}{V_{out}} \times 100 &= \frac{g \times e_{A2}}{\sqrt{2} \times g \times V_{in}} \times 100 \\ &= \frac{e_{A2}}{\sqrt{2} \times V_{in}} \times 100 \\ &= \frac{81 \times 10^{-9}}{\sqrt{2} \times 0.025} \times 100 \\ &= 2.3 \times 10^{-4} \end{aligned}$$

These percentages are minuscule and would not influence our measurements. Hence the op-amp noise calculation would deem this op-amp as suitable for the use of amplifying the measured signal.

The input bias current of this op-amp is a maximum of $6\mu A$. The bias current produces a DC voltage of [15]:

$$V_{in} = I_b(R_{in} \parallel R_f)$$

Where $R_f \approx (R_{in} \parallel R_f)$ as $R_{in} \approx \infty$. Using these $R_f = 2.2M\Omega$ and $I_b = 6\mu A$ we get a $V_{in} = 13.2V$ which will distort the measured AC signal by hitting the supply rails of the op-amp. In order to remedy this we connect the equivalent resistance, $R_f \approx (R_{in} \parallel R_f)$ in series with positive input and ground as shown in figure 3.17. This ensures that both inputs sees the same DC driving resistance thus reducing the DC voltage created by the input bias current to a small common-mode voltage.

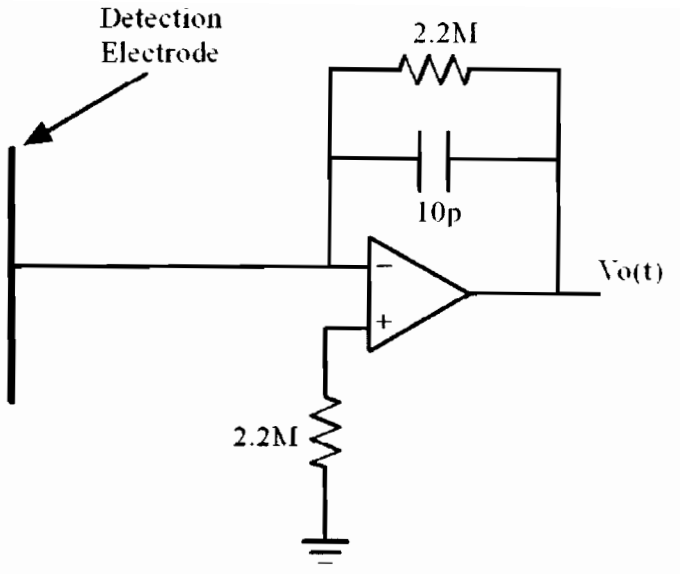

Figure 3.17: Input bias current correction

3.4.2 Multiplier and Low Pass Filter

The multiplier used for the phase synchronous detection was a Analog Devices Low Cost Analog Multiplier, AD633 [1]. The multiplier had a $1MHz$ bandwidth. The equation governing the device is:

$$W = \frac{(X_1 - X_2)(Y_1 - Y_2)}{10} + Z$$

Where X_1, X_2, $Y_1$and Y_2 are the analog input signals and Z is an additional summing input. We used it by connecting X_2, Y_2 and Z to ground, ie. 0 Volts. Leaving us with $W = \frac{X_1 \times Y_1}{10}$ as the output. X_1 was connected to the amplified measured signal and Y_1 to the signal used for phase synchronous detection. Y_1 would switch between the I and Q sinusoidal signals.

The low pass filter did not require a high speed op-amp as we were only interested in the DC component of the signal. So we used a replica of an LF351 which was a Texas Instruments JFET-Input Operational Amplifier, TL081 [6]. The op-amp has low power consumption, and low input bias and offset currents, it has a GBP at $3Mhz$ which is more than sufficient.

3.4.3 Switches

The switch used in the circuit was a Maxim Quad SPST switch, MAX445 [4], with a maximum off-leakage current of $5nA$. If our input voltage was a $5V$ signal we would have effectively a $1G\Omega$ off resistance. This resistance value translated into an equivalent capacitance will give us $1.3fF$ which is less than 3% of the smallest expected interelectrode capacitance. So in order to prevent any crossing of the signal we arranged one

switch package, which contained 4 SPST switches, as a T-switch. This would then leave one switch unused. To secure the isolation we took it a step further by creating two T-switches per channel as discussed before. On the secondary switch package we used the fourth unused switch to control the switching in of the measurement circuitry. This is all shown in figure 3.14 (see switch linked to control line Do).

We also used one of these MAX445 switches to control the switching in of I and Q channels. The switch has a maximum turn on time on $250ns$ which is more than sufficient for the rate at which we are going to switch. It also has a logic supply voltage pin which enables it to be TTL compatible when attached to a $5V$ line.

3.4.4 Decoder and Hex inverter

The switching of the driving signals is done via a decoder that controls the switches as discussed. Due to the fact the actual signals were not being routed through a multiplexer but instead through switches made a decoder perfect for the job. The decoder we used was a SGD-Thomson HC4514, 4 to 16 line decoder. It is high speed with a typical switching time of $18ns$. It has an inhibit pin allowing all the outputs to be held low at any one time. It uses a 4 input binary code to select a high level output at any one of the sixteen outputs. The decoder runs off a supply,V_{cc}, of between -0.5 to$7V$ which enables it, according to the data sheet, to have an output voltage at V_{cc}. This output level is sufficient to control the switches if V_{cc} is kept at $5V$ or above.

We designed the decoder to work in conjunction with a hex inverter. This enable the logic signals to be inverted. The hex inverter we used was a Texas Instruments CMOS Hex Inverter, CD4069. The hex inverter came in a package that contained six inverters. So we need to use three of these inverters to cover all the outputs of the decoder. These inverters were used for the anti-phase switching of the T-switches. Using all the outputs of the decoders and the hex inverters we would require 32 control lines going to our circuitry in order to control the driving signal.

Chapter 4

Hardware Implementation and Testing

4.1 Technical Difficulties

4.1.1 Electrode Design

In order to create a device that would pass signal through the DUT we needed to design an electrode that would create electric field lines that would cut across the path of the DUT only. In order to do this we needed to make sure that the electric field lines did not spread outside the ring in which the DUT was placed. As shown in figure 2.18 we can see that the electrodes are placed in a circular manner around the DUT. Electric field lines would then extend from the driving electrode to the other electrodes which are held at virtual earth via the negative input of the trans-impedance amplifier. If we take a look at figure 4.1 we can see how the field lines can travel in the opposite direction from the DUT, this would result in reduced sensitivity of the DUT, and may also introduce errors resulting from objects close to the DUT. In order to prevent this we created an earth shield behind each electrode forcing the field lines that were generated behind the electrode to ground. In this way any field lines that spread from one electrode to the next would have to exist within the circular area.

Our first attempt in creating such a device included the use of a cookie tin as shown in figure 4.2. We grounded the cookie tin causing a barrier between the external world and the device under test. We then mounted electrodes on rubberised stilts and connected them via a coaxial cable to the measurement circuit. This approach was fine as a prototype for initial testing but contained a few flaws. The DUT was limited to what could fit inside the relatively small tin, which had a diameter of 17cm. The electrodes did not at first have inter-electrode shielding causing the electric field lines to jump from one electrode to the next directly. Even with the inter-electrode shielding in place the electric field line isolation was not good enough. Due to this we needed to redesign the electrode system.

The approach we took in order to combat the coupling of electric field lines from adjacent electrodes was to make each electrode individually. We created an earth housing for each electrode. Then we placed the electrode inside it and connected the housing to earth

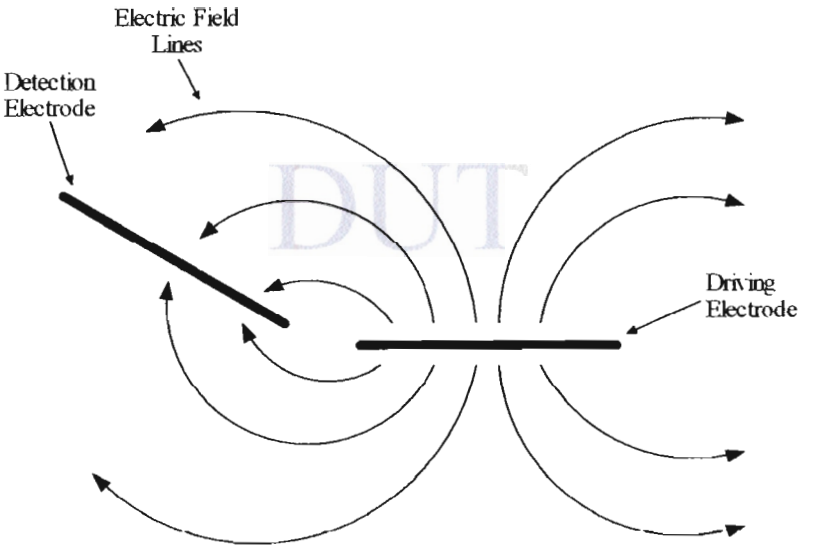

Figure 4.1: Electric field lines without exterior shielding

Figure 4.2: Earth shielding with cookie tin

and electrode to the circuit via a shielded coaxial cable. The electrode was separated from the earthed housing by using a sheet of plastic the same size as the electrode. The configuration can be seem in figure 4.3. If we take a look at the electric field lines as shown in figure 4.4 we can see that they have to travel through the DUT and they can not couple with each other through the outside.

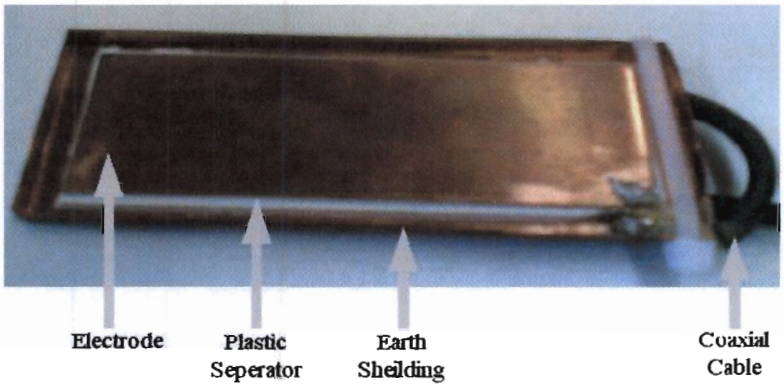

Figure 4.3: Individual Electrode Housing

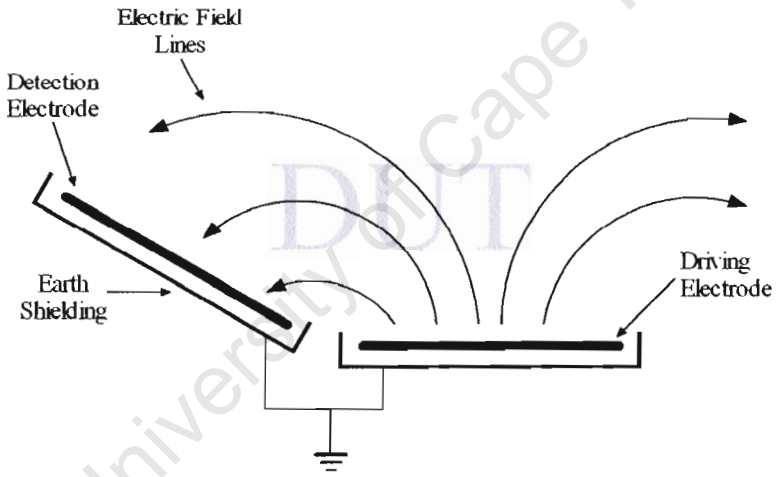

Figure 4.4: Electric Field Lines after individual housing

4.1.2 Practical Aspects

PCB Board Design

As in the case of the electrode design the printed circuit board also had to be carefully designed in order to accommodate the high susceptibility to electric field coupling. In order to combat this we took two approaches. The first was the actual layout of the circuitry in the channels and the other was the shielding.

As discussed in the previous chapter, each of the channels contained the following circuitry as shown in figure 4.5. Here we can see that the driving signal has to be fed to both

the electrode and the phase synchronous detector. But in order to feed both these points the strong drive signal has to pass the sensitive trans-impedance amplifier even when the channel is in detection mode. Switch IC 1 is used to switch in the driving signal or isolate it (using three of the switches in a T configuration). Switch IC 2 is used to further isolate the signals (again using three switches in T configuration). Switch 2 also has the function of switching in the measurement circuitry (using the fourth switch in the package).

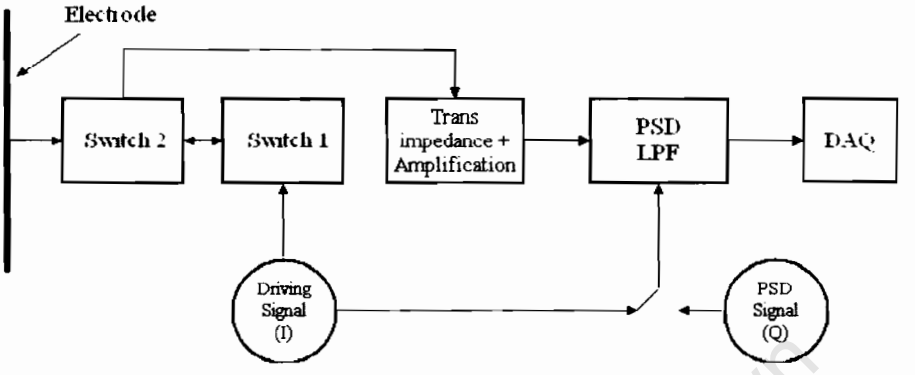

Figure 4.5: Block diagram of channel circuitry

In order to prevent the driving signal from having to be routed past the trans-impedance amplifier we rearranged the physical layout of the chips in figure 4.5 to figure 4.6. Here we can see that switch IC 1 is placed between the amplifier and phase synchronous detector. In this way the driving signal is attenuated by the first T-switch, in switch IC 1, when in detection mode, therefore allowing the signal that is measured to be amplified first before passing any other strong signals.

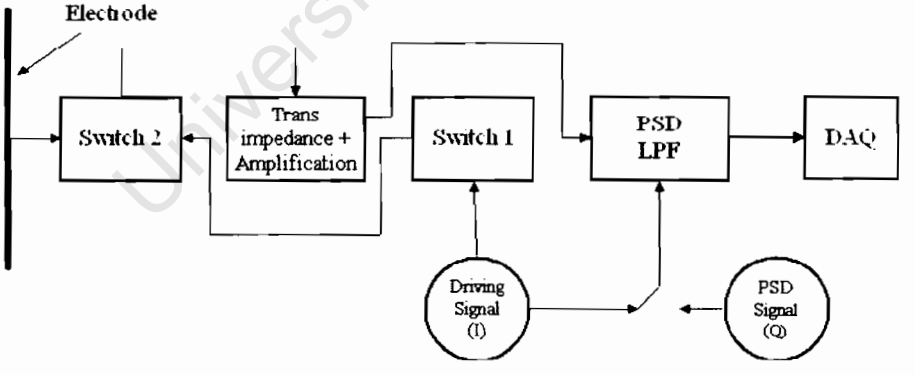

Figure 4.6: Modified block diagram showing the order of the physical layout of the channel circuitry

In the initial design of the measurement circuitry we included two phase synchronous detectors and two LPF in order to measure both I and Q channels simultaneously. It was later realised that this was only possible for a system with eight or fewer electrodes due to the fact that the DAQ only had 16 analog inputs. For an 8-electrode system we would have 16 measurements which would take up all of the DAQ's inputs. It was at that stage

that we incorporated the switch that would control the signal multiplication of the phase synchronous detector as shown in figure 3.11. A PCB was then layed out containing eight parallel channels. Two such boards were manufactured and components soldered in place.[1]

Another problem that we faced was the coupling between channels on the actual board. It gave rise to a similar problem faced by the electrodes without shielding. When initially testing the board the channels adjacent to the driving channels would saturate to the maximum the op-amps allowed. Even the channels two along from the driving electrodes would give false readings. It was later realised that the driving signal when used to drive an electrode would couple into the detection circuitry of the adjacent electrode channels as shown in figure 4.7. In order to prevent this we took similar approach as before. We placed an aluminium ground sheet below the circuit board, (between which was placed a sheet of plastic). We then needed to individually shield the channels from each other. This was done by using an aluminium foil coated sheet of paper that was insulated on the one side with support strips to create an earth barrier between the sensitive parts of the circuitry. Once each of the signals was isolated from one another the circuit functioned satisfactorily and the end result was similar to that of figure 4.4. The signals carried to and from the electrodes were shielded from one another by using earth screened coaxial cabling.

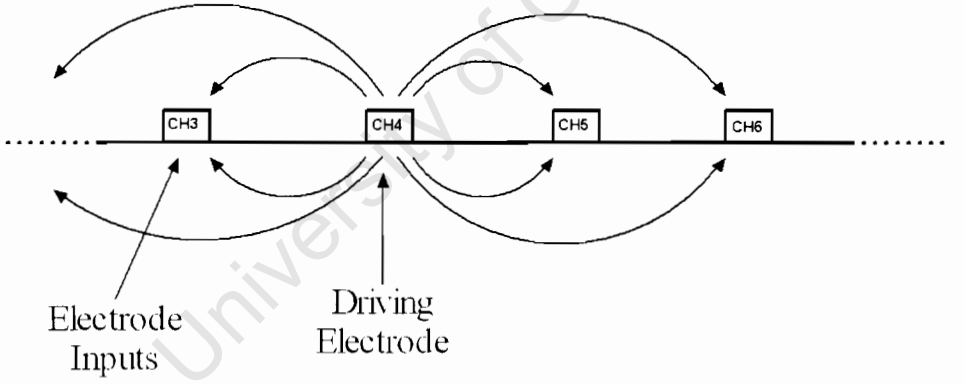

Figure 4.7: Front view of circuit board with coupling electric field lines

A photograph of the actual measurement circuitry can be seen in figure 4.8. Here we can see the actual placement of the chips as well as the redundant phase synchronous detector and LPF. In figure 4.9 we can see the material used to isolate the channels from one another, including the ground plane.

4.2 Data Capturing

In this section we will cover the process in which the the data is captured and stored. The data capture involves three components:

[1]The author wishes to acknowledge and thank Mr EW Randal for laying out the PCB artwork.

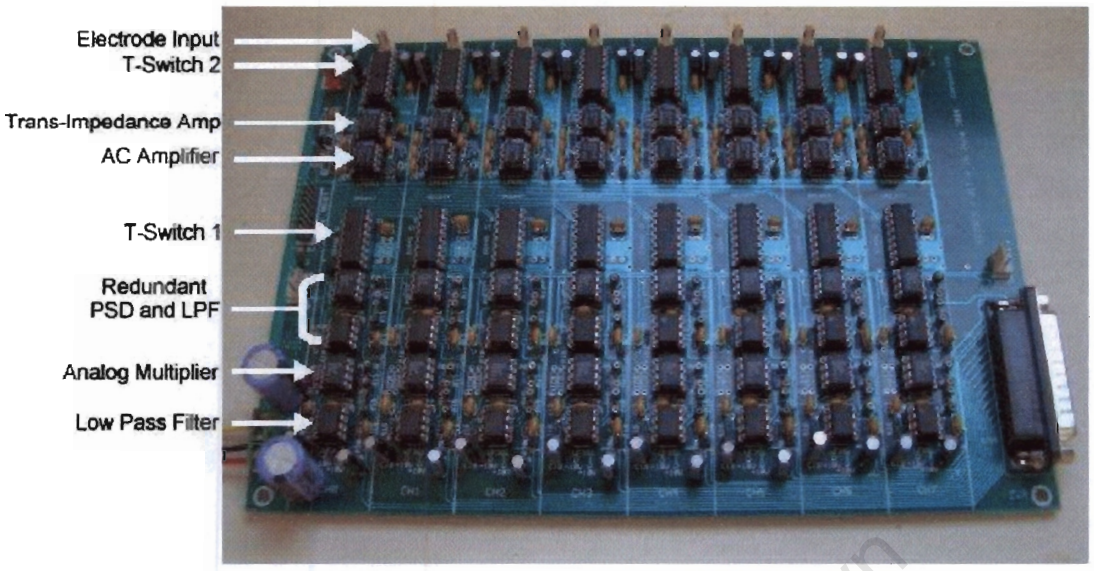

Figure 4.8: Photograph of actual measurement board

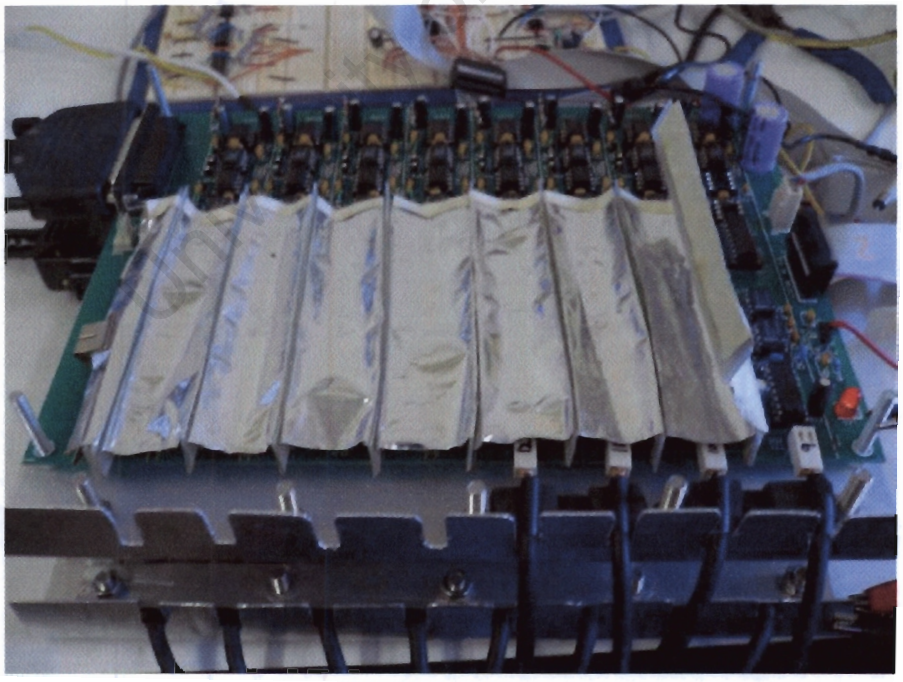

Figure 4.9: Circuitry with shielding and ground plane

1. The actual board used to measure the data.
2. The multiplexing circuitry to select the driving and detection electrodes as well as the phase synchronous detection switching.
3. The DAQ which controls the manner in which the above two will behave.

As shown in figure 3.9 and figure 3.11 we require seven digital signals to control the behavior of the circuit. Five of these lines are used to control the decoder, four for selecting the drive signal and one for selecting the inhibit function. The other two signals are used to switch in either the I or the Q channels for phase synchronous detection. The code used to control the whole measurement process is written in Matlab and consists of numerous processes and functions, enabling us to setup the DAQ and modify the data as it is read in by the system. The code can be seen in Appendix A.

The main code that calls up all the other functions can be seen in Appendix A.1. In this section of the code we declare the number of electrodes in the system, determine the number of calibration frames to be taken and call on the function to initialise the card, capture the data and reconstruct the image.

In order for us to acquire the data from the DAQ we need to initialise the card and setup up the proper parameters. This code is shown in Appendix A.2. As we can see from the code we need to declare the number of analog input, analog output, digital output channels required before we can use any of them. In the case of the analog inputs we need to specify a sampling rate in which to capture the data. The DAQ that we used has an analog input sampling frequency of $1.25MHz$, but we do not require such high speeds due to the limitations of the LPF and other components. We then needed to tell the DAQ how many samples to take per trigger. This is the number of samples stored per channel for any one set of measurements. The signal to noise ratio can be improved by averaging a batch of samples over a period of time. The total dataset aquisition time is a function of the time spent intergrating samples and hence is a trade off with the signal to noise ratio.

As we are going to be generating the I and Q channels using the DAQ we were required to specify the signals before hand. Here we were limited by the DAQ's $1MHz$ clock dedicated for the analog outputs. If we were to generate two sinusoidal signals we needed to use an even number of samples, where $\frac{n}{4}$ is the number of samples used to shift the signal by exactly $90^o$and n is the number of samples used in a cycle. We are limited by $\frac{n}{4}$ in that the n has to be multiples of 4. If we produce a sinusoidal signal with 4 samples per cycle we would end up with a triangular waveform. The frequency of this wave form would be $\frac{1MHz}{4} = 250KHz$. This is a good frequency but the signals produced would be very poor in shape. If we take the next number of samples we have a frequency of $\frac{1MHz}{8} = 125kHz$ where $n = 8$ which is a decent frequency at which to work. The shape of the signal produced also resembles a sinusoidal much better than a triangular waveform as shown in figure 3.12. This signal is shifted by $\frac{n}{4} = \frac{8}{4} = 2$ samples to the left in order to produce a 90^o phase shifted version of thee signal. Due to the fact that both the signals

are identical in samples except for the phase shift we can be assured that the signal on the output of the LC filters would have similar amplitudes and would be 90^o out of phase. After the signals are setup up mathematically they get queued in a buffer waiting for a trigger command to enable the output.

Once the DAQ has been initialise it is ready to start capturing data. The first step as shown in the main code A.1 is to get calibration data from the system. This is done in two stages. The first stage is to collect measurements of the actual component's offset values. This is done by enabling the inhibit pin on the decoder allowing none of the electrode to drive the signal. These offset reading are very small (typically between -0.03 and $+0.01$ Volts) and can be seen in figure 4.10. The next step is to take a data set of a either healthy pole or of a homogeneous medium such as air from which to calibrate the system. Once these are measured and stored the we can move on to taking measurements of the desired objects.

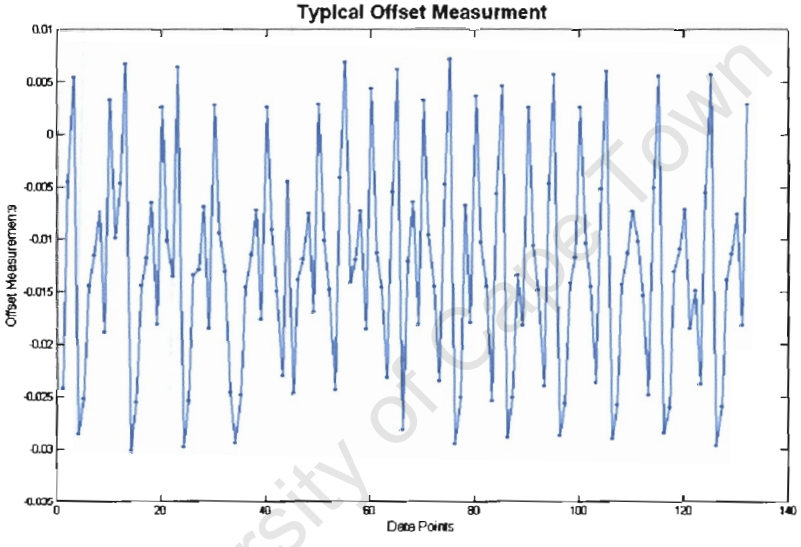

Figure 4.10: Data set of offset reading

The measured data would follow the same capturing procedure of the calibration data set, the only diffirence would be that is will be in a continuos loop updating the reconstructed image and the captured data. As we explained before the data is captured in a sequence. If we have N electrodes, we will drive on electrode 1 and measure on electrodes 2 to N, then drive on electrode 2 and measure on electrodes 3 to N and electrode 1, and so it will continue until we have reached the Nth electrode. The number of measurements taken can therefore for calculated using the formulae, $N(N-1)$. The measurements are in two loops, one controlling the I and Q measurements and the other the drive electrodes. Within the loops we compensate with pauses for the settling times of filters and switching. The capturing sequence measures the data for driving electrode 1 while using the I channel for phase synchronous detection. It then stores this data into a vector. It then moves onto electrode 2 and add its measured values to the end of the vector. This is done until all the I channel phase synchronous detection data is store in one long vector. It does

the same measurements while using the Q channel for phase synchronous detection. We found it simpler to measure all the analog inputs including the driving channel which is of no use due to the fact that it is not measuring any data while that channel is driving. So it captures the N measurements for a driving electrode in a vector and then adds the next drving electrodes measurements to the end of the first vector. It continues creating this vector until all the measurements for all the driving electrodes has been stored in one long vector. Now we have a vector that is N^2 long for both I and Q. We then take these vectors and divide it into sets of N measurements per vector placing each driving electrodes vector in its own row starting with electrode one being the first row of a now $N \times N$ matrix. Now we shift each row's data in such a way that the first column would contain the irrelevant data from the driving electrodes channel. This allows for a uniform repetition of the data from driving electrode in a full circle to the last or adjacent to driving electrode. The data values in each column would now be relatively similar to each other even though the electrode numbering is different. After we create this $N \times N$ matrix we discard the irrelevant information in the first column, and create a new $(N-1) \times N$ matrix. We then rearrange this matrix back into a new vector where we can see a repetitive pattern for every $N-1$ measurements. A typical measurement dataset can be seen in figure 4.11. After the matrix manipulation we end up with a single vector that is $N(N-1)$ long which contians both the I and Q channel data in the form $a + jb$. This whole matrix manipulation can be seen in Appendix A section A.3.

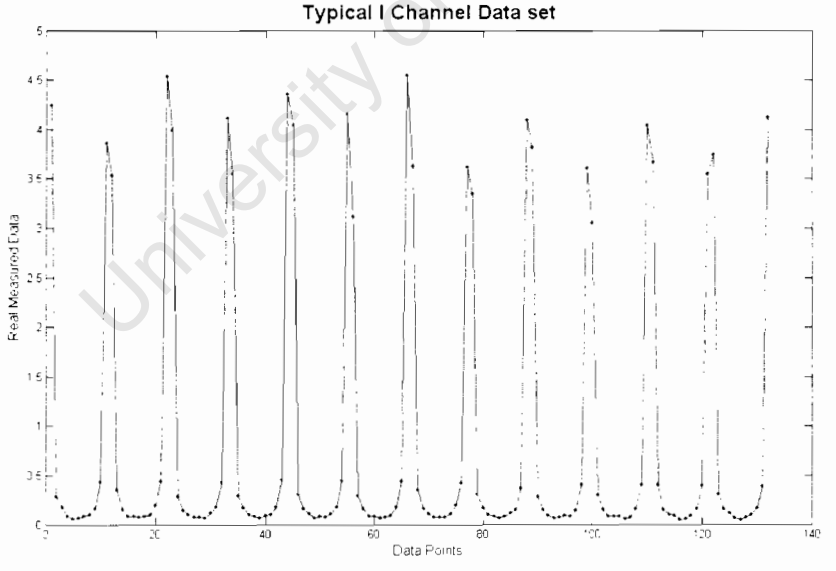

Figure 4.11: Typical dataset of the I channel

Once the data for a complete cycle, driving on all the electrodes and doing phase synchronous detection for both I and Q channels, is stored, we move onto the next stage of the code, the image reconstruction. This process will be explained in the next chapter as well as the initial results.

Chapter 5

Image Reconstruction and Testing on Various Objects

5.1 Analysis of Data

In order for us to process the data, we need to ensure that the actual measurements are true and not random or erroneous. In order to do this we calculate the standard deviation of the data sets. The following information was derived from data sets where each value is the average of 80 samples over a period of 0.02 seconds. The channel was allowed to settle prior to this for a time for 0.016 seconds. A frame is a dataset as shown in figure 4.11. The total time taken to acquire one frame is 0.432 seconds. The standard deviation was then calculated from 10 frames. So now we have a matrix of 132×10, where 132 is the number of measurements in one frame in a 12 electrode system and 10 is the number of frames we are using to calculate the standard deviation. Each column would refer to a particular set of measurements between a driving electrode and the receiving electrode. Matlab was used to calculate the standard deviation of each column which was plotted below the actual data. This can be seen in figure 5.1 which corresponds to a typical result. The standard deviation is calculated using the formula:

$$\sigma = \sqrt{\frac{\Sigma(x_i - \mu)^2}{N - 1}}$$

Where σ is the standard deviation, x_i is the value of the ith sample, μ is the mean of the samples in that sample set and N is the number of samples. In essence the standard deviation uses the mean of the samples captured to calculate an approximation of the average variation for any sample within the set. The bottom graph in figure 5.1 contains the calculated standard deviation for the 10 samples taken for each measurement.

If we take a closer look at figure 5.1 as shown in figure 5.2 we can see that the 5th measurement has a relative high value of standard deviation compared to its neighbours. We can use the actual data, $0.09V$ and the calculated value of the standard deviation,

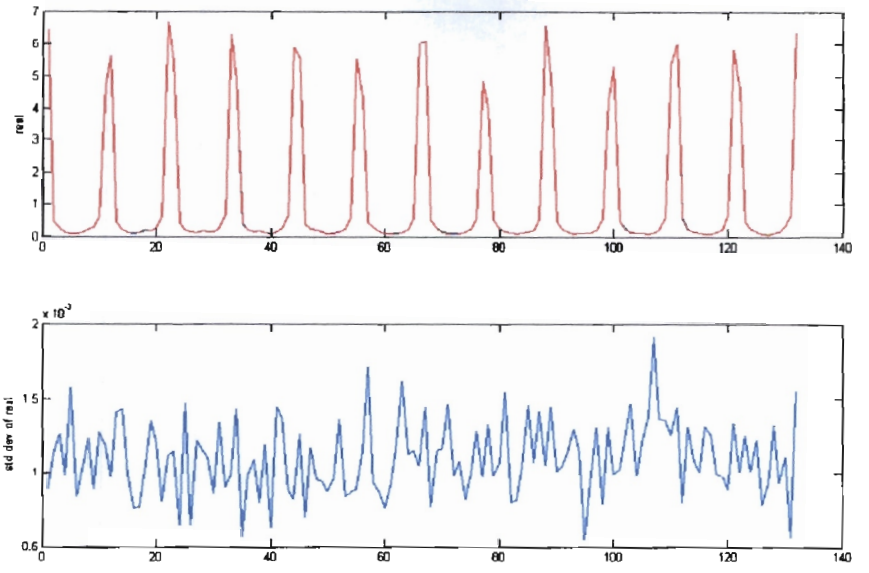

Figure 5.1: Plot of real data set with its standard deviation

$1.6 \times 10^{-3}V$ to calculate the percentage deviation for this sample

$$\begin{aligned} P.D. &= \frac{\sigma}{x} \times 100 \\ &= \frac{0.0016}{0.09} \times 100 \\ &= 1.8 \end{aligned}$$

Where $P.D.$ is the percentage deviation, σ is the calculated standard deviation and x is the value of the sample. From the above calculation we can see the the percentage deviation for the 5th sample is about 1.8%. In a measurement system with measurements so small this deviation can be considered as good and acceptable. This percentage was calculated using the best combination for the highest value of standard deviation with lowest measured signal amplitude we could find. This would mean that any other value is likely to have a smalled percentage deviation. If we take a higher sample value of 6 the performance measure would be

$$\begin{aligned} P.D. &= \frac{\sigma}{x} \times 100 \\ &= \frac{0.0016}{6} \times 100 \\ &= 0.02 \end{aligned}$$

showing us that the higher the value of the sample the smaller the percentage deviation.

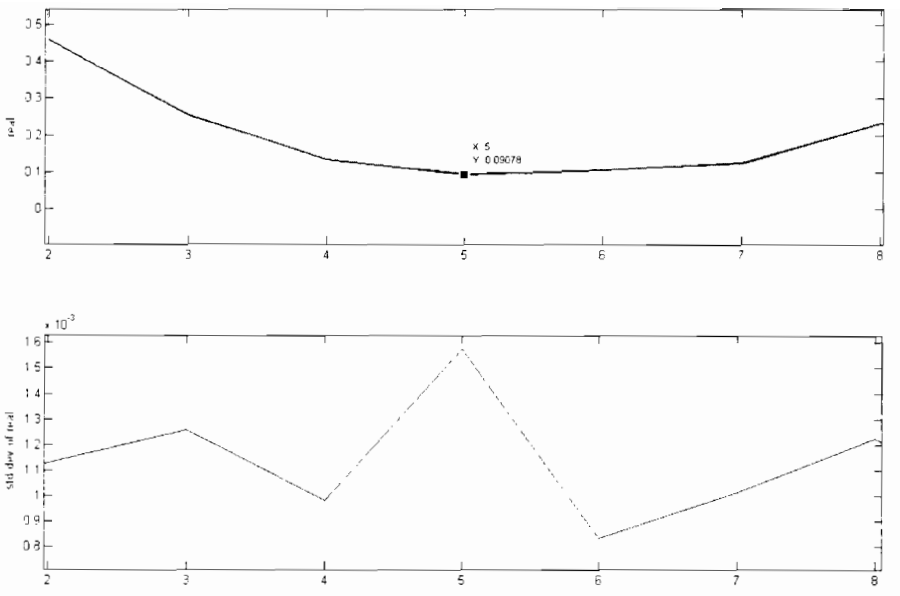

Figure 5.2: Closer look at real data and its standard deviation

5.2 Image Reconstruction

The image reconstruction algorithm used for processing the data was based on a regularized least-squares approach [17], implemented in MATLAB by my supervisor, A.J.Wilkinson. The MATLAB algorithm was initially developed for 2-D conductivity imaging using ERT [29], and then adapted for 2-D permittivity imaging using ECT. Measurements taken with our developed EIT measurement system on dry wood samples were found to be dominantly capacitive, and hence it was concluded that an ECT algorithm would be suitable for processing the data[1]. The reconstructed images presented in this thesis are thus images of the permittivity distribution in a 2-D plane of the electrodes.

In essence, the regularised least-squares algorithm aims to obtain the permittivity distribution $\varepsilon(x, y)$ for which the measured data set (i.e. currents measured at the sense electrodes) best matches that predicted by accurate simulation, and subject to a smoothing contraint (referred to in as 'regularisation') [17]. The simulator, or 'forward model', uses the finite element method on a grid of triangular elements, to solve Poisson's equation

$$\bigtriangledown \cdot [\varepsilon(x, y) \bigtriangledown \phi(x, y)] = 0$$

for the potential distribution $\phi(x, y)$ subject to the boundary conditions, being the voltage on the driving electrode, and the virtual earths on the detection electrodes. The current through the detection electrodes is then computed from the potential distribution.

[1] It may be possible that in some cases, the measurements would not be dominantly capacitive (i.e. the measured current phasor has both real and imaginary components). For such cases, being true EIT, the appropriate algorithm would reconstruct the permittivity and conductivity images from the complex data.

The regularised least-squares formulation involves minimising a cost function, which is usually carried out using a Newton Raphson optimization algorithm [17]. For qualitative imaging, however, a single iteration is sufficient, and may be used to produce a fast algorithm for real time imaging [29]. The images displayed in this thesis are thus qualitative permittivity images, for the assessment of the potential of the developed EIT hardware for permittivity imaging in the intended application. Investigation of the performance of more accurate interative algorithms was not carried out as part of this work, but is identified as a topic for future research.

5.3 Preliminary Testing on Objects within a Perspex Tube

In order to test the system we attached the electrodes to a perspex tube with a diameter of $200mm$. The electrodes were arranged in sequence and were adjusted to be equidistant from each other. The perspex tube with the electrodes attached can be seen in figure 5.3.

Figure 5.3: Perspex tube used for testing various objects

As you can see the electrodes are held in place by an elastic belt looped through an additional copper plate added to the earth screen. The system would now be calibrated with the electrodes firmly placed against the tube with nothing inserted. Once the calibration measurements are taken we can insert objects into the air space within the tube.

5.3.1 Images created by using wooden objects

By inserting a wooden object into the space we were hoping to achieve a sense of the systems sensitivity and image accuracy. A $50mm$ wooden pole was first inserted into the middle of the space as shown in figure 5.4. We then triggered the capturing of the data, using an air calibrated data set to reconstruct the image. The results of the reconstructed image can be seen in figure 5.5. In the image the scale on the right hand side corresponds to the reconstructed permittivity, relative to the calibration reference (which was air), where 1 is the calibrated value or empty space. Therefore most of the image has a value of 1 due to the fact that it is empty and corresponds to the calibrated values. The peak value at the centre reached about 1.9.

Figure 5.4: $50mm$ Wooden Pole place in the center of the Perspex Tube

In our next test we inserted two halves of a $100mm$ wooden pole inside the space. We placed them a slight distance apart in order to test the sensitivity of the system to objects that are close to each other. The placement and size of the poles can be seen in figure 5.6. We followed the same procedure as with the reconstruction of the $50mm$ pole and used the same calibration data. The reconstruction results can be seen in figure 5.7. The results clearly show the two objects separately resolved. Here also we can see the rest of the image settling on the calibrated value of the empty space. In these two reconstruction we can see on the right hand side scale within the image that the wooden objects appears as a value more than 1. This is due to the fact that wood has a higher dielectric constant than that of air. Values for dry wood reported in the literature are from 3 to 5 [19].

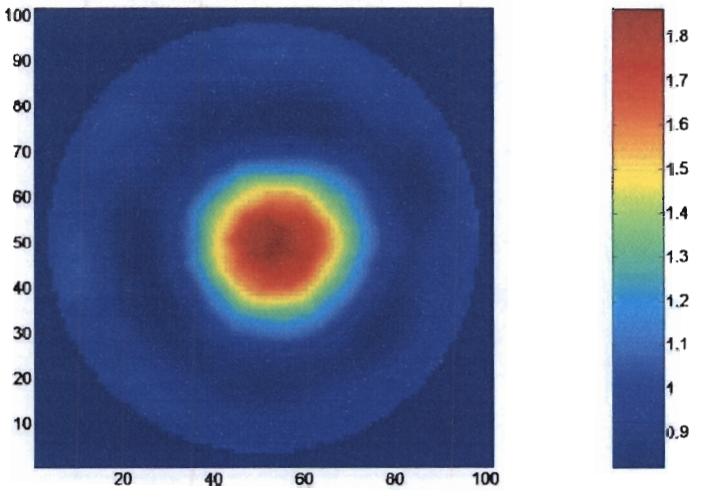

Figure 5.5: Reconstructed Image of the $50mm$ Wooden Pole placed inside the Perspex Tube

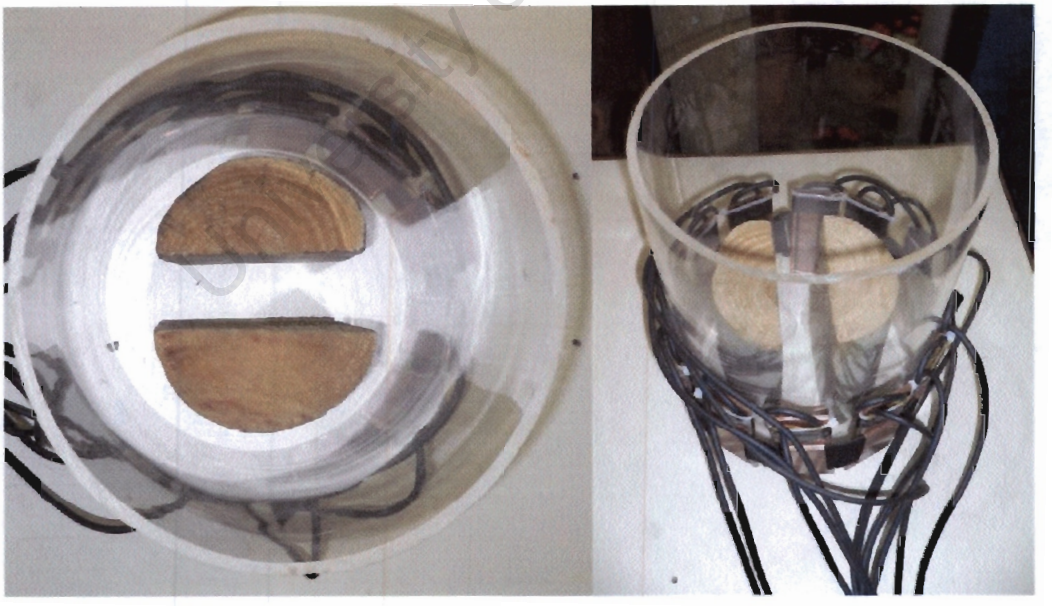

(a) (b)

Figure 5.6: Image of two pole halves spaced within the Perspex Tube

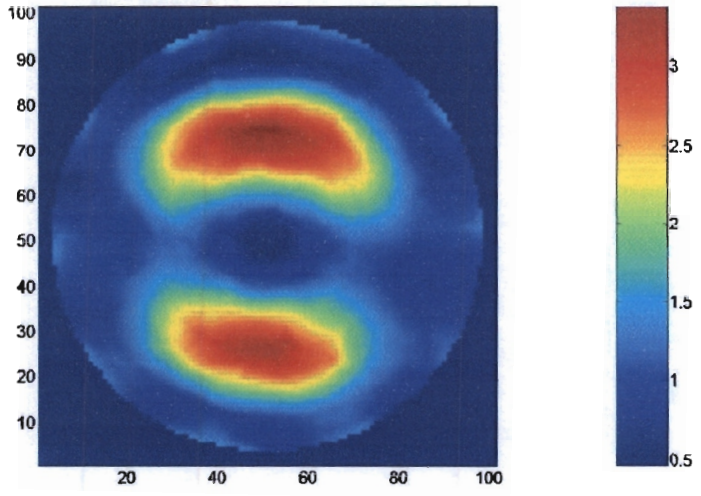

Figure 5.7: Reconstructed Image of two pole halves placed inside the Perspex Tube

5.3.2 Images created using non wooden objects

Now that we have tested that the system works with wooden objects we needed to test it when we insert an object with known higher dielectric constants than that of wood. For the test we used a bottle of glycerol and a bottle of de-ionised water. Both of these object has a much higher dielectric constant than that of wood and air. In the first test we placed a bottle full of glycerol just off-centre from the tube as shown in figure 5.8. A reconstruction of this can be seen in figure 5.9. As we can see the bottle which has been placed off center is shown as off center in the reconstructed image. Similar results can be seen for the de-ionised water used in figure 5.10. In figure 5.11 we can see the image of two plastic object insert into the area under testing. The object at the bottom of the jar is a plastic rod and the object on the top is a holder of gluestick. The reconstruction shows the objects location quite accurately. The scale on the reconstruction suggests the items have a very low permittivity, under 1.5, but still the image appears quite sharp. It is noted that the resolution of the system is only about 11% of the diameter, thus images of objects smaller than this will under estimate the permittivity of the object. These initial tests suggest that the system would be sensitive enough, and with sufficient resolution for the intended application.

5.4 Testing on Wooden Pole Models

In order to assure the working of the system with objects completely made of wood we bought several wooden poles normal used for building timber samples. The building timber bought were treated and accurately machined wooden poles. They had radial cracks but other than that they were perfect cylindrical specimens. We took two poles of diameter $180mm$ and had holes of different sizes drilled into them. The drilled holes were used to simulate the rot that would normally occur in the real poles. We drilled the timber

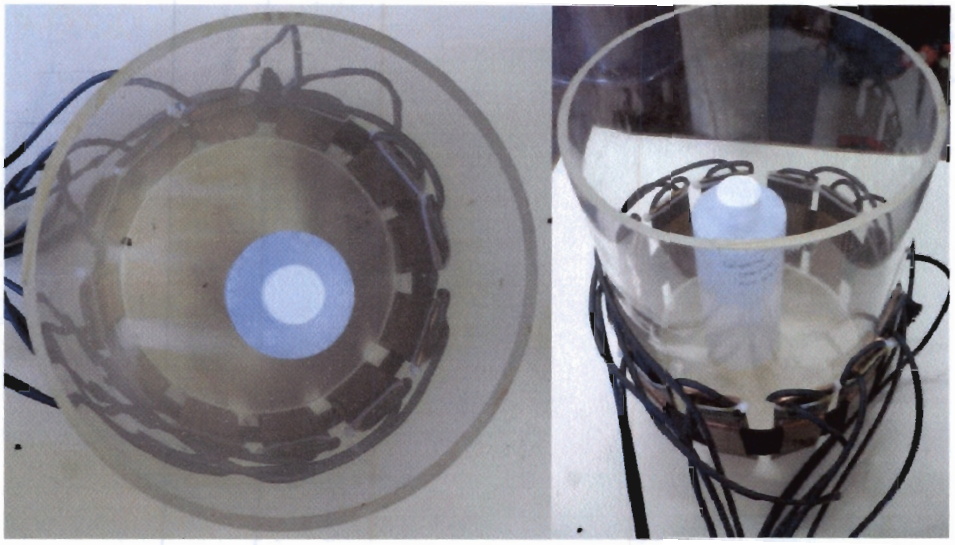

(a) (b)

Figure 5.8: Images of a bottle of glycerol place inside the testing area

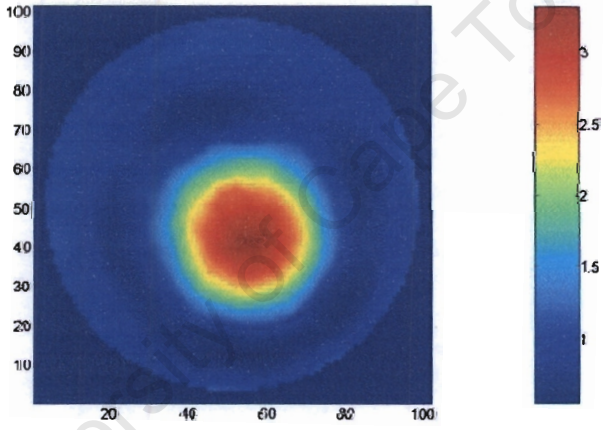

Figure 5.9: Reconstructed Image of the glycerol bottle

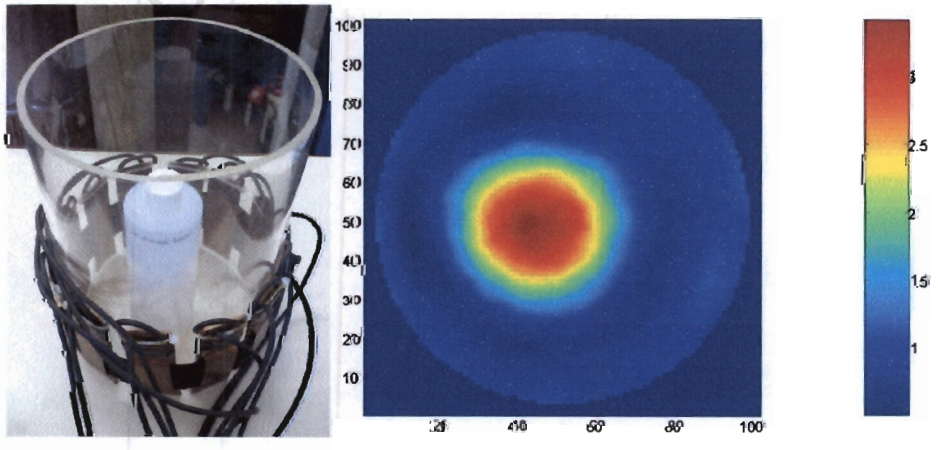

(a) (b)

Figure 5.10: Image and reconstruction of a bottle of De-ionised water

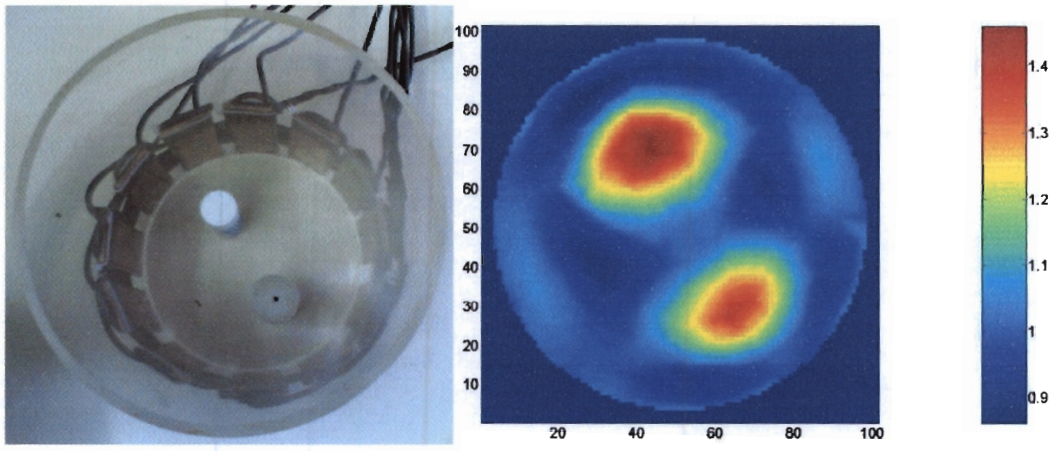

(a) (b)

Figure 5.11: Image and reconstruction of two plastic objects inserted into the perspex jar

with two different hole sizes. The first consisted of a hole that was $50mm$ in diameter and the second a hole of $100mm$ in diameter. In addition to the $180mm$ timber purchase we purchased similar poles of diameters $50mm$ and $100mm$ in order to plug the recently drilled holes. With the hole plugged the system would think that the pole was completely solid and healthy.

In our first test we strapped the electrode around the pole with the $50mm$ hole and plugged the hole with the $50mm$ pole as shown in figure 5.12a. We then calibrated the system on this plugged pole and reconstructed an image of the output. The output looked solid as if the pole had no hole as shown in figure 5.13. We then remove the pole and the reconstructed image took the exact shape and was comparable in size to the $50mm$ hole as shown in figure 5.14.

The same test was performed for the pole with the $100mm$ hole drilled though the center. We first plugged the hole then calibrated the system. Thereafter we removed the plug and imaged the hole. The pole with the hole and the plug can be seen in figure 5.15a. The reconstruction of the hole can be seen in figure 5.16b. We can see from the image of the reconstruction that the $100mm$ hole seems a bit larger but to most extent resembles the original hole. One thing that we can notice in both reconstruction, $50mm$ and $100mm$ holes, is that the actual hole is depicted as a lower number than the solid wood in the scale on the right. This is because we are now working on a wood calibration compared to the previous tests where we calibrated with air. With the air calibration our empty space was measured as one on the scale. With the wood models the solid wood is measured as one and the air is the lower value. The air becomes a lower value due to the fact that air has a lower dielectric constant than that of wood, eg. $Air = \varepsilon_o$ and $Wood = 5 \times \varepsilon_o$, therefore on the image the $Air\ Value = \frac{1}{5} = 0.2$.

These images were taken on almost perfect samples of wood. The electrodes that were placed on the pole did not have to be moved (to a different pole) after calibration since the plug could just be removed. This aided in the excellent reconstructed images that were

(a) Hole Plugged (b) Hole Unplugged

Figure 5.12: $180mm$ pole with a $50mm$ hole drilled through the center

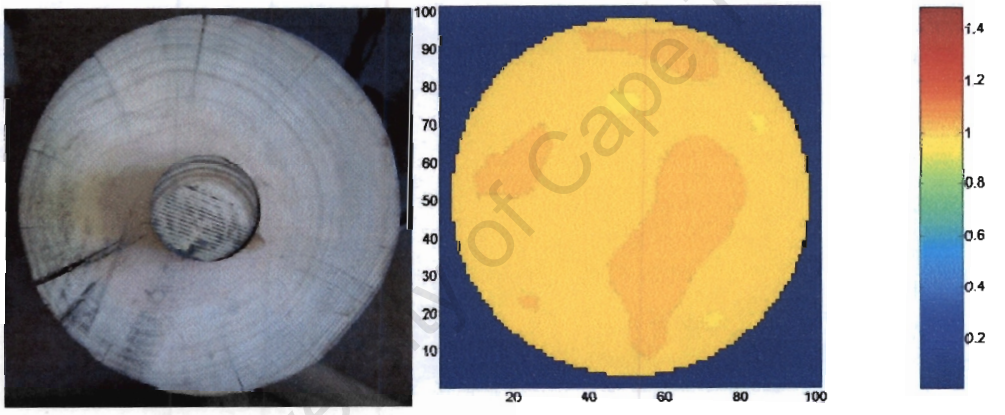

(a) (b)

Figure 5.13: Top view of $180mm$ pole with hole plugged and reconstructed image

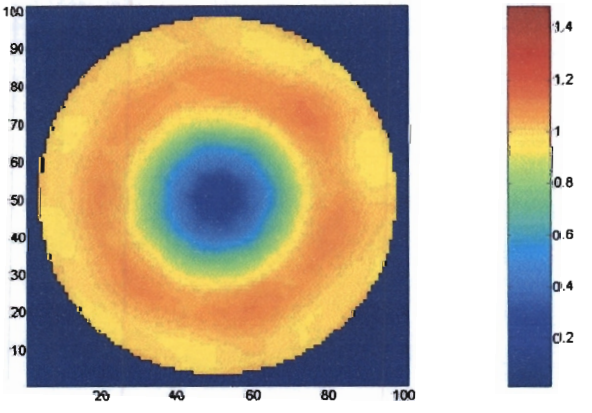

Figure 5.14: Reconstruction of the $180mm$ pole with the $50mm$ hole

created. On a real wooden pole the outer edges are not as smooth as the machined poles and the calibration has to be done on a known solid piece of wood. This means that the electrodes will have to be removed from the calibrated pole and then placed on the test specimen after the calibration has been done. This would lead to misplaced electrodes where the spacing cannot be recreated exactly. We will test this theory in the next chapter where we will present the results of testing the system on actual rotten poles.

(a) Hole Plugged (b) Hole Unplugged

Figure 5.15: $180mm$ Pole with a $100mm$ hole drilled through the center

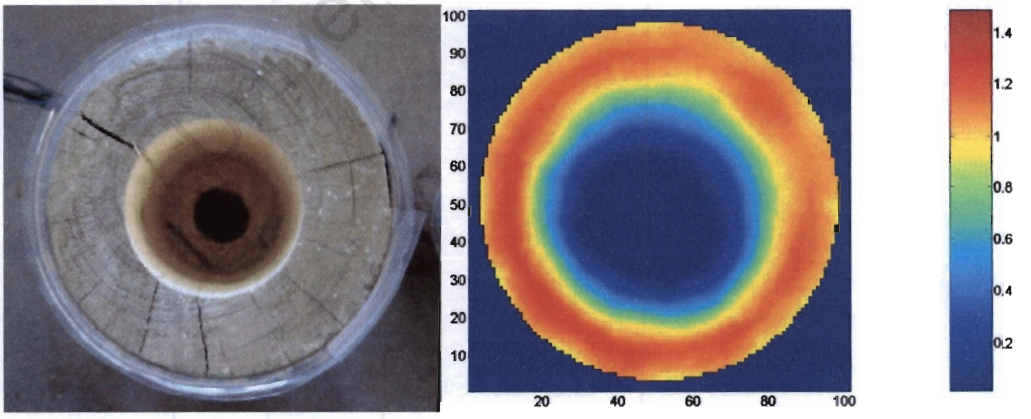

(a) (b)

Figure 5.16: Top view and reconstruction images of the $100mm$ hole

Chapter 6

Testing on Wooden Poles

6.1 Field Trip to Rawsonville

In August of 2004 we travelled to Rawsonville, just outside Cape Town. We were informed that a distribution line had been decommissioned and that the replacement poles were currently being installed. We saw this as an opportunity to experience first hand the problem that we aimed to solve. We gained valuable information and samples from the trip. This enabled us to study and develop the system further in order to accommodate for the actual problem. We discovered that the poles had a base diameter of between $250mm$ to $300mm$ as shown in figure 6.1. The measurement instrument would therefore need to be built with a certain flexibility due to the varying size of the poles. Hence we used the elastic band with the electrodes attached to it.

(a) (b)

Figure 6.1: Base diameter images of new replacement poles

Some of the poles we encountered, which had been removed and were lying on the ground allowing inspection of the base, were either termite or water damaged. On most of the damaged specimens the outer shell still remained hard whereas the core became soft and flaky which can be clearly seen in figure 6.2. An example of the termite and water damaged poles can be seen in figure 6.3. The average life span for the distribution poles is

between 30-50 years depending on climate and location. Several typical samples were cut using a chain saw and transported back to our laboratory.

Figure 6.2: Soft Inside Core of a Rotten Pole

(a) Termite Damaged Pole (b) Water Damaged Pole

Figure 6.3: Damaged wooden poles

6.2 Testing on Field Pole Specimens

The final testing phase was to produce images using actual field sample poles that we collected from Rawsonville. The two samples that were used for testing were segments approximately 1.2m in length, cut above and below ground. One of which had approx-

imately 50% above ground and 50% of it below ground whereas the other had approximately 20% above ground and 80% below ground. The section above ground was where the pole was relatively healthy and solid and the part below ground where the rot and holes started to develop. We can clearly see the distinguishing line that separates the two parts of the pole in figure 6.4. The method in which the testing took place was to calibrate the system on the healthy part of the pole then move the electrodes to the unhealthy part for comparison. This would sort of emulate the same approach we used with the machined poles in the previous chapter. The only problem that might occur would be the realignment of the electrodes as we need to detach them and move them whereas in the previous tests they remained stationary. Numerous attempts were used to keep the electrodes stationary such as the development of a plastic jacket that was used to strap the electrodes around in order to enable it to slide up and down the pole. This did aid us in the sliding of the electrodes but due to the knots in the poles and the irregularities in the shape, the electrodes would still shift around.

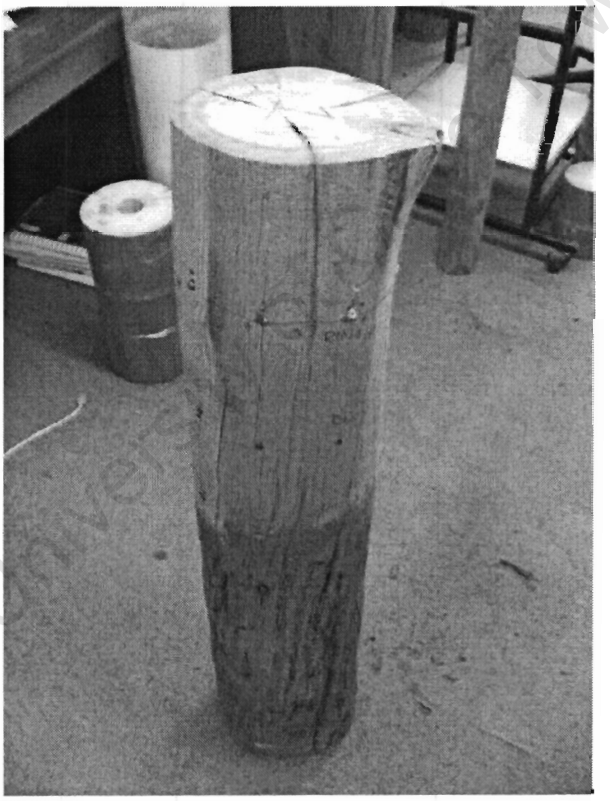

Figure 6.4: Side view of a pole showing the ground line (Pole 1)

We will call the pole in figure 6.4 as "Pole 1". This pole was the initial test subject. The band of electrodes were strapped around the healthy section of the pole as shown in figure 6.5a and then moved onto the middle, ground line, and unhealthy region as shown in figure 6.5b and c respectively. The results for the calibration on the healthy section of Pole 1 can be seen in figure 6.6. We can see the the image values are one as the wood is now be the calibrated medium. Now we slide the electrodes to the ground lying

position as shown in figure 6.5b. The images produced from this section of the pole can be seen in figure 6.7. We can see that the edges are still around the one region of the scale which would be considered healthy but the center which now contains majority blue is in the bottom end of the scale. As explained before, with the wood calibration, any air gaps will be depicted as less that than one. In the position shown in figure 6.5c we get the reconstruction as shown in figure 6.8. We can clearly see from the photo that the reconstruction is accurate in that the air filled center in the photo is now the blue center in the reconstruction. The accuracy of the images is dependant on electrode position and calibration data. If the electrodes are shifted alot we get errors in the measurements as shown in the figures below. The red fringing can be based on the fact that the electrodes may shift closer to on another as we slide the mechanism up or down. The calibration data is taken on a section that is assumed to be healthy since we cannot see within the actual pole. If an air gap is calibrated into the data then we would get erroneous readings in that air gaps in that particular area would be reconstructed as healthy.

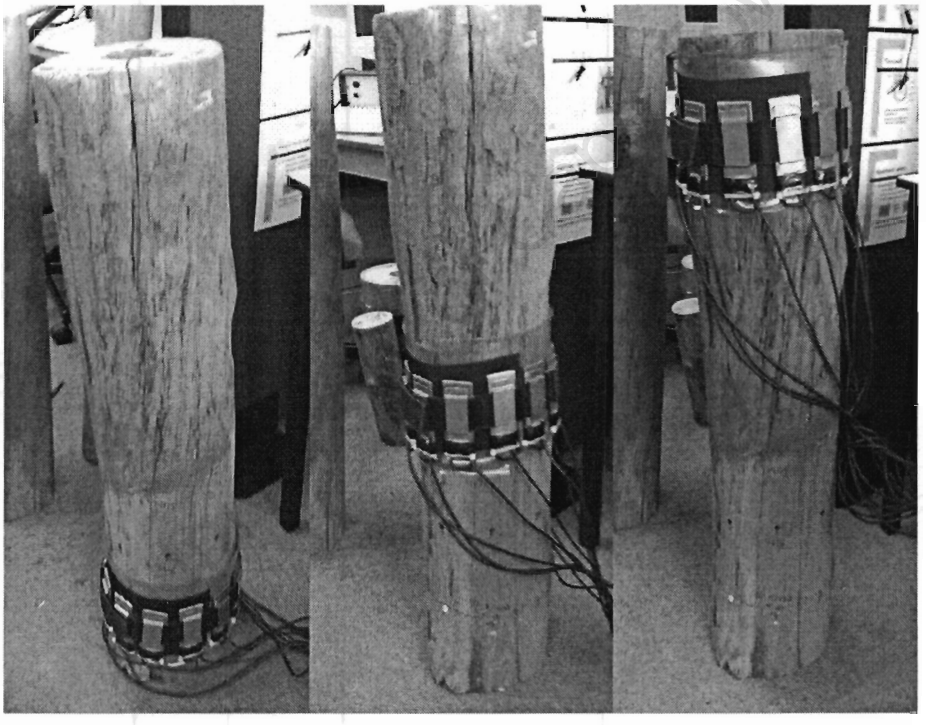

(a) Healthy Level (b) Ground Level (c) Rotten Level

Figure 6.5: Electrode positions on Pole 1

In an aid to accurately understand the wooden medium we used an air calibrated data set to reconstruct the above images again. By this I mean that we strapped the electrode around the perspex tube took the calibration readings and then strapped it onto the pole and took the measurements without a recalibration. The results can be seen in figure 6.9a, b and c for the healthy, ground and unhealthy section respectively. In these reconstructions the scale is much higher due to the air calibration. Any solid wood would therefore appear as a higher number on the scale. In figure 6.9a we can see that most of the image appears to be

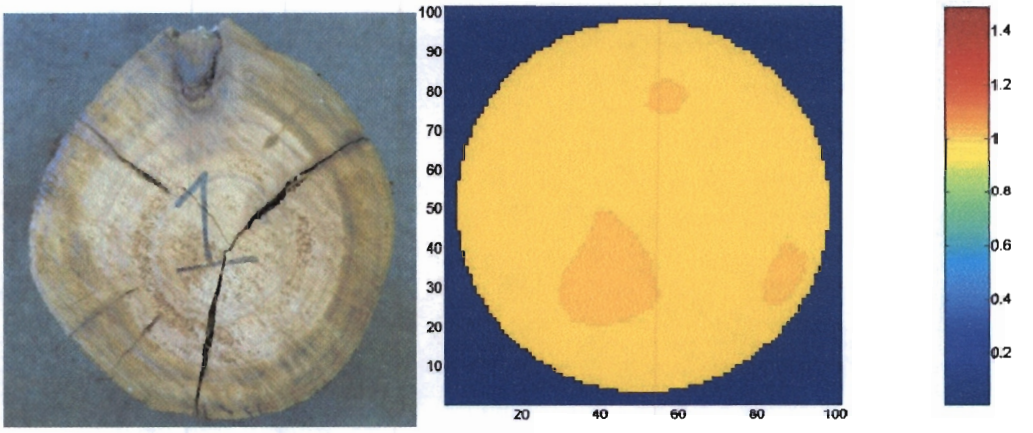

Figure 6.6: Images of the healthy level of Pole 1

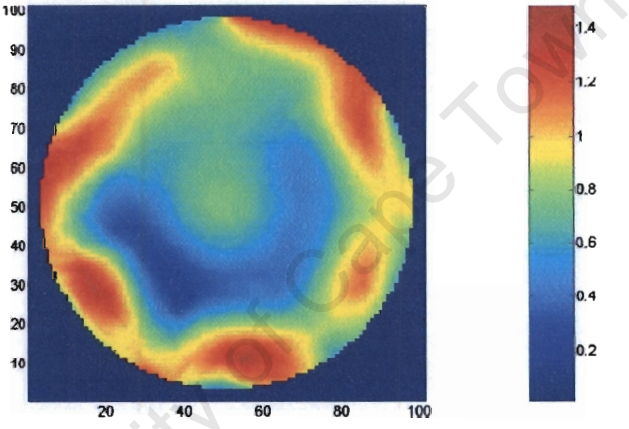

Figure 6.7: Ground lying reconstruction image of Pole 1

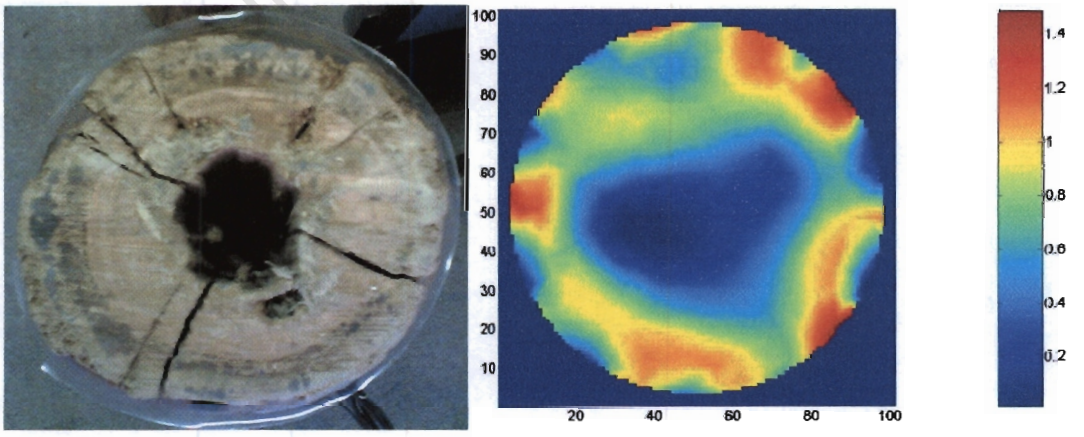

(a) (b)

Figure 6.8: Images of the rotten section of pole one

above one but the center appear to be higher that the rest of the image. This could lead us to understand that the density of wood is not as homogeneous as that of air and therefore appears to have a higher permittivity towards the center. But even with deduction we can see that in figure 6.9b the image scales toward one which suggests that the pole has more air inside it and in figure 6.9c the center appears to be air which would correspond with the image of the unhealthy section.

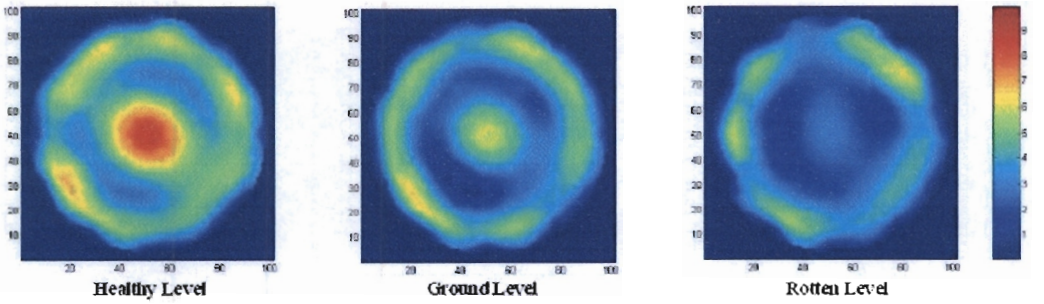

Figure 6.9: Reconstruction images on pole one using air calibration

We did the same test on a secondary pole, referred to as "Pole 2". This pole did not have as much rot as Pole 1 as shown in figure 6.10. Pole 2 can be seen in figure 6.11 as well as the positioning of the electrodes for the various tests. The results of the wood calibration can be seen in figure 6.12. As would be expected the closer we moved to the unhealthy section of the pole the lower we move on the scale signifying air gaps or less dense wood. The reconstructed images from figures 6.12 and 6.8 clearly shows us that the imaging of rot in real wooden poles does indeed work. From figure 6.12 we can see that even though the pole did not have a distinct hollow, the system was able to pick up that the medium was less dense, ie. containing more air, and therefore reconstructed the image accordingly. This with further study can be used to determine the strength of the pole. We can also note that even though the images created using the air calibrated data of Pole 1 can be analysed to give us the proper information needed, the wood calibration is a more direct measurement of the density that is applicable to that wooden pole. The results are promising but do have certain flaws such as the electrode positioning and calibration. These flaws can be ironed out and will be dealt with in the recommendations chapter.

(a) Top (b) Bottom

Figure 6.10: Top and bottom images of Pole 2

(a) Healthy Level (b) Ground Level (c) Rotten Level

Figure 6.11: Electrode placements on Pole 2

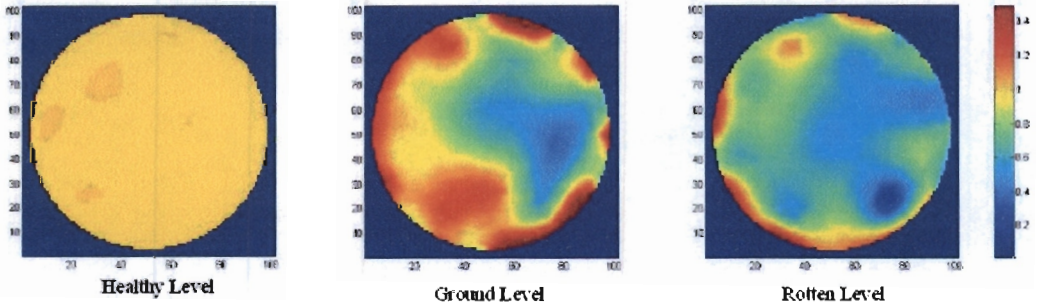

Figure 6.12: Reconstruction images of Pole 2 using wood calibration

Chapter 7

Conclusions

The initial project was to produce an EIT device capable of detecting rot non-destructively in wooden poles. The results in the previous chapter have proven that we can detect defects and rot within the poles. The method that we used to build the device was with the initial help of the AC based capacitance tomography system as discussed in the literature survey. We used the AC based system's design and modified it in order to suite the scope of the project. The method involved the injection of a sinusoidal signal through a medium and measuring the phase shift and amplitude of that signal on the detection electrodes (via the synchronous detection method). Due to the large spacing between the electrode plates the signal received by the trans-impedance amplifier was drastically attenuated. By choosing the right components and determining the appropriate level of accuracy we were able to produce a device that was able to detect changes within the femto Farad range. This proved to be sensitive enough in order to detect slight changes in the permittivity of the wooden poles. The system followed a routine measuring procedure whereby the pole is wrapped with electrodes and the signal is driven by each electrode one at a time while measuring the voltages on the detection electrodes. This enabled us to produce an image of the inside of the pole using a tomographical reconstruction algorithm.

The system although being sensitive enough to detect changes within the femto Farad range, had some flaws. The system had a slow frame refresh rate due to the settling of the LPF and the capturing of the samples. The images produced with the perspex jar and the machined poles seemed near perfect, but as mentioned before this was due to electrodes being kept in the exact same place as the calibration readings. The images of the actual poles did not come out as well as the previous images due to the fact that the electrodes had to be moved and not the pole or the objects. The surface of the wooden poles onto which the electrodes were mounted was not always smooth and contained knots and gaps. The poles were not always circular and therefore left uneven gaps of air while shifting the electrodes into a new position. None the less the overall image still managed to produce the desired results.

The system as shown in the images can be used as more than just a device to detect rot in wooden poles but also as a device that can detect nearly any object within its calibrated

frame. The sensitivity was also proven by the insertion of plastic objects into the air calibrated perspex jar. Due to the low permittivity of plastic, close to one, we were assured that any object with higher permittivity would give us better results. This was shown when we inserted the wooden pole halves and the bottles of de-ionised water and glycerol. The scale for these objects was clearly higher and more pronounced that that of the plastic objects indicating their higher permittivity.

So in conclusion we have designed a system which is not only sensitive enough to detect rot in wooden poles but a system that is versatile to be used in many other areas of study involving impedance tomography.

Chapter 8

Recommendations

As mentioned before the system does have a few flaws and many of them with further study and preparation can be avoided or fixed. Here is a list of recommendations that might enable the system to function with greater accuracy and ease.

- The LPF of the system was designed to be a first order filter. This meant that we need to select a relative low frequency to ensure that only the wanted signals got through. With the aid of a second order filter we would be able to increase the speed of the filter due to the higher roll off. This would enable a faster frame rate for real time viewing of the results.

- The device used to strap the electrodes onto the DUT consisted of a belt loop and a broad piece of elastic with velcro. This served okay for stationary testing but as soon as the testing point needed to be moved the system would shift the electrodes around giving us less accurate images. In order to prevent this a bracket would need to be designed. Possibly a rigid circular jacket that would contain a depth adjustable electrode. In this way the electrodes could be adjusted to fit numerous diameters without having to shift the electrodes around.

- Test the system on real wooden poles using a fixed electrode system. The pole under test will not have direct contact with the electrodes and therefore we would not have the electrode shifting problem. One method of testing this could be to insert a wooden pole slightly smaller than the diameter of the perspex tube. This would enable us to reconstruct images of different scenarios using simulated rot. If the testing is proved to be effective the above recommendation will hold true.

- The first revision of the circuit board contained a few errors. These errors plus a few additions and removals will be necessary for the second version. A few of the changes would be to leave out the redundant PSD and LPF. We would also need to space the measurement channels a bit further from one another enabling us to produce a rigid isolation system that would shield the electrodes from one another.

- The reconstruction algorithm can also be modified to enable the use of various electrode sizes. This would enable more realistic images when object occur near the edge of the DUT.

- In order to make the system capable of testing in-situ wooden poles the whole system would need to be made portable. This can be accomplished by using a USB DAQ in conjunction with a laptop. All the required circuitry would also need to be mounted in a carry case with easy to insert plugs for the electrodes, power and measured signals. A slight problem might arise from the fact that USB DAQ's normally does not have high frequency analog outputs. In this case an analog signal generator would need to be designed in order to produce both the I and Q channels.

Appendix A

A.1 Main code

```
% EIT main script
% eit_data_capture.m
% Script to capture datasets and display waveforms
% 18 Jan 2005, FS & AJW% EIT main script
% Script to capture datasets and display waveforms
%
%clc
% Set up NI card
%
N_electrodes = 12;
N_measurements = N_electrodes*(N_electrodes-1);
do_cal = input('Do calibration ?  (y/n)','s');
N_frames_to_ave = 4;
% NB Must be greater than 1 for column averaging to work
if ((do_cal=='y') | (do_cal=='Y'))
% Capture reference data for calibration
% Get offsets
fprintf('Reading offsets\n\n');
offsets_frame_store = zeros(N_frames_to_ave,N_measurements);
fig_offsets = figure;
pause(0.5);
[dio,ai,ao] = initialise_ni_card();
signal_on = 0;
for n=1:N_frames_to_ave
[data_frame] = get_data_frame(N_electrodes,signal_on,dio,ai);
% Store nth frame in a matrix
offsets_frame_store(n,:)  = data_frame;
real_min = -0.2; real_max = 0.2; imag_min = -0.2; imag_max = 0.2;
fig_title = sprintf('Offsets Frame n = %d',n);
plot_data_frame(fig_offsets, data_frame,fig_title,...
...real_min,real_max,imag_min,imag_max)
end
offsets_frame = mean(offsets_frame_store); % Take average
real_min = -0.2; real_max = 0.2; imag_min = -0.2; imag_max = 0.2;
fig_title = 'Offset frame';
plot_data_frame(fig_offsets, offsets_frame,fig_title,...
...real_min,real_max,imag_min,imag_max)
% Get reference frame in air
calibration_frame_store = zeros(N_frames_to_ave,N_measurements);
fig_calibration = figure;
pause(0.5)
[dio,ai,ao] = initialise_ni_card();
signal_on = 1;
```

```
for n=1:N_frames_to_ave
[data_frame] = get_data_frame(N_electrodes,signal_on,dio,ai);
% Store nth frame in a matrix
calibration_frame_store(n,:)  = data_frame;
real_min = -1; real_max = 10; imag_min = -10; imag_max = 10;
fig_title = sprintf('calibration Frame (air) n = %d',n);
plot_data_frame(fig_calibration,data_frame,fig_title,...
...real_min,real_max,imag_min,imag_max)
end
calibration_frame = mean(calibration_frame_store);
real_min = -1; real_max = 10; imag_min = -2; imag_max = 2;
fig_title = 'calibration frame (air)';
plot_data_frame(fig_calibration,...
...calibration_frame,fig_title,real_min,real_max,imag_min,imag_max)
% SAVE OFFSETS AND CALIBRATION DATA
save offsets_frame.mat offsets_frame
save calibration_frame.mat calibration_frame
end
% NOW CAPTURE DATA OF INTEREST
%x = input('Press Enter to capture data');
fig_data = figure;
pause(0.5);
N_frames = input('Enter number of frames:  ');
signal_on = 1; % Signal control 1=>on 0=>off
dataset = zeros(N_frames,N_measurements);
[dio,ai,ao] = initialise_ni_card();
pause(1)
avi_filename = 'movie.avi'; % AVI file
FPS = 1; % frames per second
mov = avifile(avi_filename,'FPS',FPS);
%Nfigrows = 1;
%Nfigcols = 3;
for n=1:N_frames
[data_frame] = get_data_frame(N_electrodes,signal_on,dio,ai);
% Store nth frame in a matrix
dataset(n,:)  = data_frame;
real_min = -1; real_max = 10; imag_min = -2; imag_max = 2;
fig_title = sprintf('Frame n = %d',n);
%plot_data_frame(fig_data, data_frame,fig_title,...
...real_min,real_max,imag_min,imag_max)
%pause(0.01)
save dataset.mat data_frame
%plotnum = mod(n-1,Nfigrows*Nfigcols)+1;
%subplot(Nfigrows,Nfigcols,plotnum);
tomonrm_one_step_Fayaaz;
F = getframe(gca);
mov = addframe(mov,F);
end
mmm = close(mov); % Close avi file
% Save data to disk
save dataset.mat dataset
% Ascii file
dataset_real = real(dataset);
dataset_imag = imag(dataset);
save -ascii dataset_real.txt dataset_real
save -ascii dataset_imag.txt dataset_imag
```

A.2 Initialisation of the NIDAQ

```
function [dio,ai,ao] = initialise_ni_card()
%
% Function to initialise NI card for EIT measurments
% FS & AJW
% 18 Jan 2005
% INPUTS
% OUTPUTS:
% dio - digital io structure
% ai - analogue input variable
% ao - analogue output variable
openDAQ=daqfind;
for z=1:length(openDAQ),
stop(openDAQ(z));
end
%Adding analog input line
ai = analoginput('nidaq',1);
set(ai, 'InputType', 'SingleEnded');
addchannel(ai , [0:11]);
aiFs = 4000;%sets the sampling frequency per channel
ai_dt = 1/aiFs; % Spacing between samples on a channel
integration_interval = 10E-3
% Specify time period over which to integrate
% Note LPF RC time constant on LPF is 1ms.
%Setting the attributes to the Analog Input Channels
set(ai, 'SampleRate', aiFs);
samples_per_trigger = ceil(integration_interval/ai_dt)
set(ai, 'SamplesPerTrigger', samples_per_trigger);
set(ai, 'TriggerType', 'Manual');
set(ai.channel,'InputRange',[-9 10]);
set(ai, 'TriggerRepeat', inf);
%Sets up 2 analog output lines
ao = analogoutput('nidaq',1);
addchannel(ao, [0 1]);
dac_sample_rate = 1E6;
set(ao, 'SampleRate', dac_sample_rate);
set(ao, 'TriggerType', 'Manual');
set(ao, 'RepeatOutput', inf);
%sets up two signals for the analog output
N = 8;
%Since sampling rate is 1Mhz the frequency is
%determined by N eg.N=8 we have 1Mhz/8=125Khz
t = linspace(0,(2*pi)-((2*pi)/N),N);
I_drive = 3*cos(t);
%signal used for driving
%the electrodes and demodulating the in phase channel
Q_demod = circshift(I_drive,[0 -N/4]);
% Shifts the signal a quarter cycle hence a qaudrature output.
%NB Q_demod waveform chosen so that the sign of the final Q channel
is
%correct.  Q channel is -0.5sin(t)
%Adding 6 digital lines for multiplexing
dio = digitalio('nidaq', 1);
addline(dio, 0:6, 0, 'Out');
putdata(ao, [I_drive' Q_demod']);
%buffers in the sin and cos functions for output
start(ai);
% Switch on analogue I/Q cos and sine waves
start(ao); % Initialise analogue outputs and wait for trigger
trigger(ao); % Trigger the outputs - should now generate sin and cos
waves
```

A.3 Capturing a Data Frame

```
function [data_frame] = get_data_frame(N_electrodes,signal_on,dio,ai)
% Function to get one 'data_frame'
% INPUTS:
% N_electrodes - number of electrodes used
% signal_on - indicates if voltage signal is to be on or not.
% dio - digital io structure
% ai - analogue input variable
% OUTPUTS:
% data_frame - vector containing complex measurements
% signal_on = 1; % Allow drive to be switched off by putting mux to
15.
data_store = zeros(N_electrodes,N_electrodes,2);
data_vector = zeros(1,N_electrodes*N_electrodes,2) ;
final_data = zeros(N_electrodes,N_electrodes-1,2);
final_vector=zeros(1,N_electrodes*(N_electrodes-1),2);
data_matrix = data_store ;
samples_per_trigger = get(ai, 'SamplesPerTrigger');
aiFs = get(ai, 'SampleRate');
%trigger(ai); % Take readings on all channels
% Loop around and plot waveforms on screen
putvalue(dio.Line([7]),0)
%Reinitialises the inhibit pin to
%zero to allow for normal measurements
pause(0.01)
%for k=1:100 %used only when trying to calculate the std deviation
for iq=1:2
putvalue(dio.Line([5:6]), iq); % Switch in either cos or sin wave
% NOTE: 1 dec = 01 bin => cos 2 dec = 10 bin => sin
pause(0.02);
%tic
for drive=0:N_electrodes-1
% drive = Decimal number which is written to the binary mux address
if signal_on
putvalue(dio.Line([1:4]), drive) %Sets the digital output line to
drive
else
% Prevent drive voltage from reaching electrode
%(used for calibration purposes)
putvalue(dio.Line([7]),1) % Set inhibit pin on
end
% putdata(ao, [y' y1']);
% start(ao);
% Pause to allow filters to reach steady state.
% Note output R = 100E3 C = 10E-9 => T = RC = 0.001 sec
% We will wait 8 time constants, we get 1-exp(-8/1) = 0.9997
% towards steady state.
% Originally we used 100E-9 caps with a time constant of T = 0.01sec
%and we coded it to wait for 0.1 sec which was 10 time constants.
time_constant = 0.001; % RC time constant
pause(8*time_constant); % Allow filters to settle
%pause(1.5*samples_per_trigger/aiFs);
% pause for more than enough time for all readings
% NOTE: This pause may not be required if getdata waits!
trigger(ai); % Take readings on all channels
%tic
%[d] = peekdata(ai,1); % Get data from buffer
[d] = getdata(ai); % Get data from buffer
% figure(1)
```

```
% plot( d(:,1) );
% pause(0.5)
%toc
% figure;plot(d);title('d')
% Store into data vector and rearrange
data_store(drive+1,:,iq) = mean(d,1) ;
%records the data for each driving electrode in its own row
data_vector(:,12*drive+1:12*(drive+1),iq) = ...
...circshift(mean(d,1)',-drive)' ;
%data_vector takes the matrix data_store and shifts the ...
%...nth row nth places to the left aligning the corresponding channels...
%...ie.  alinging the drive channels on top of one another.
data_matrix(:,:,iq) = reshape(data_vector(:,:,iq),12,12)';
%shapes the data_vector into a data_matrix.
final_data = data_matrix(:,2:12,:); %removes the drive channels from
the data_matrix
for ctr = 1:12
final_vector(1,11*(ctr-1)+1:11*(ctr-1)+11,iq)=final_data(ctr,:,iq);
%converts the final_data matrix into a vector
end;
% corrected_vector= data_vector-shifteddcoffset2;
% cdata_matrix(:,:,iq) = reshape(corrected_vector(:,:,iq),12,12)';
%shapes the data_vector into a data_matrix.
% cfinal_data = cdata_matrix(:,2:12,:);
%removes the drive channels from the data_matrix
% for ctr = 1:12
% cfinal_vector(1,11*(ctr-1)+1:11*(ctr-1)+11,iq)= ...
...cfinal_data(ctr,:,iq);
%converts the final_data matrix into a vector
% end;
end;
%toc
end;
data_frame = -( final_vector(:,:,1) + j*final_vector(:,:,2) );
%Invert the measured readings in order to fix polarity
%[3 Inversions (inverting opamps) in the circuitry]
```

Appendix B

Detailed Circuit layouts

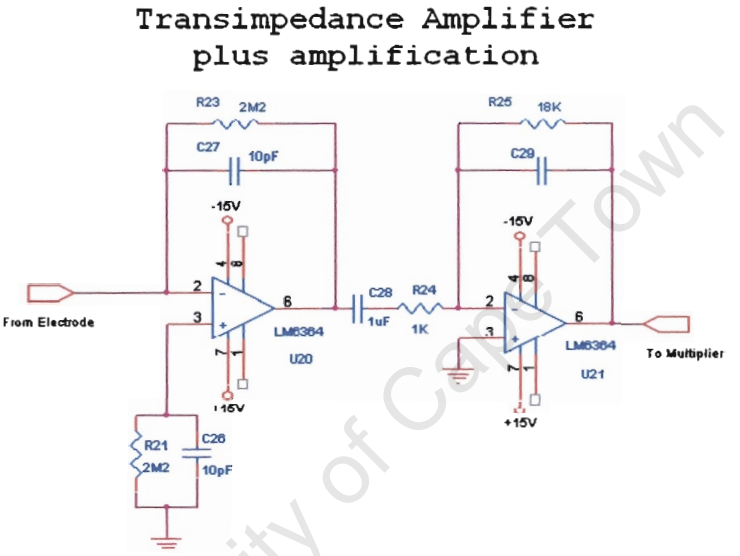

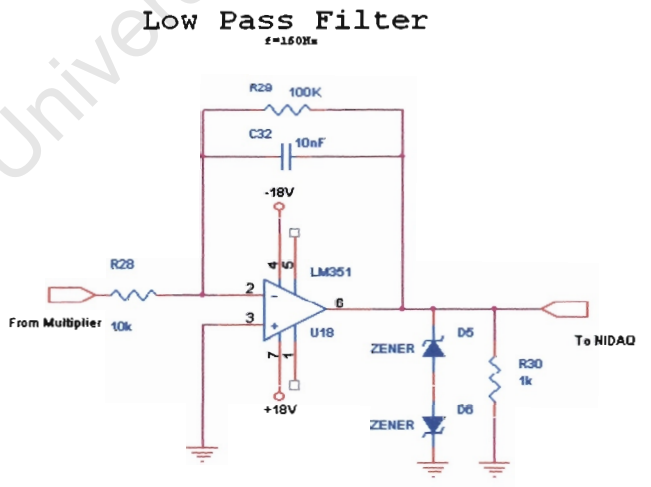

I and Q signal Switching for multiplier with LC Filtering plus drive channel filtering

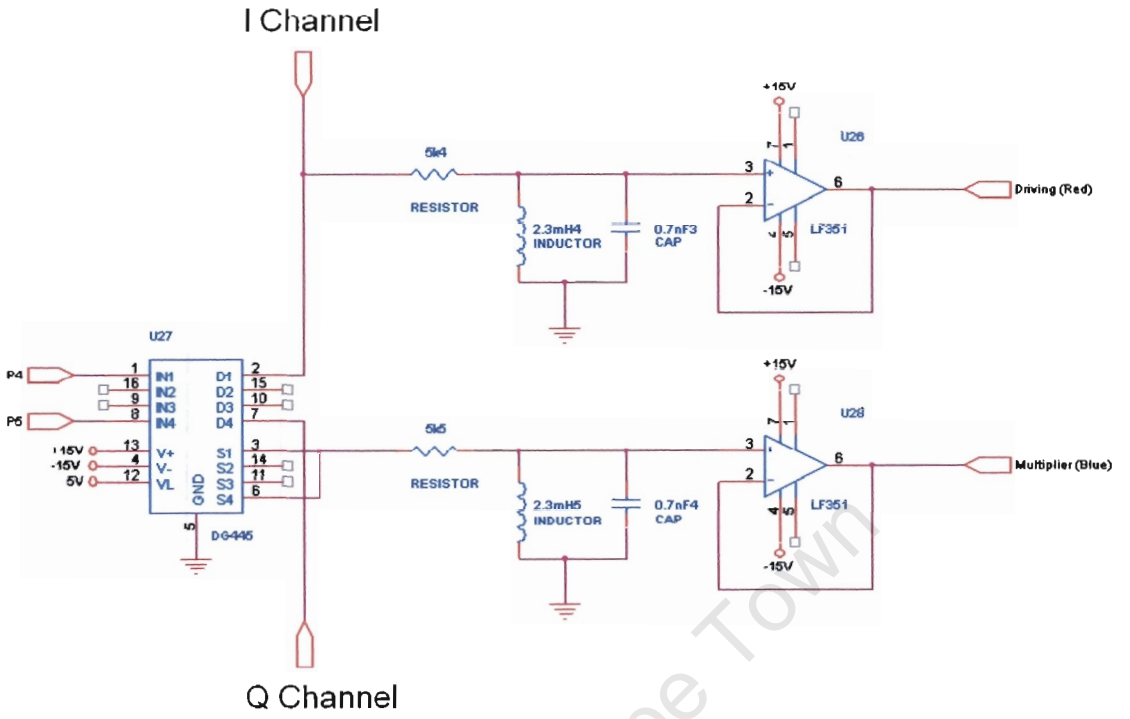

Multiplexing configuration for switching electodes into driving or detection mode

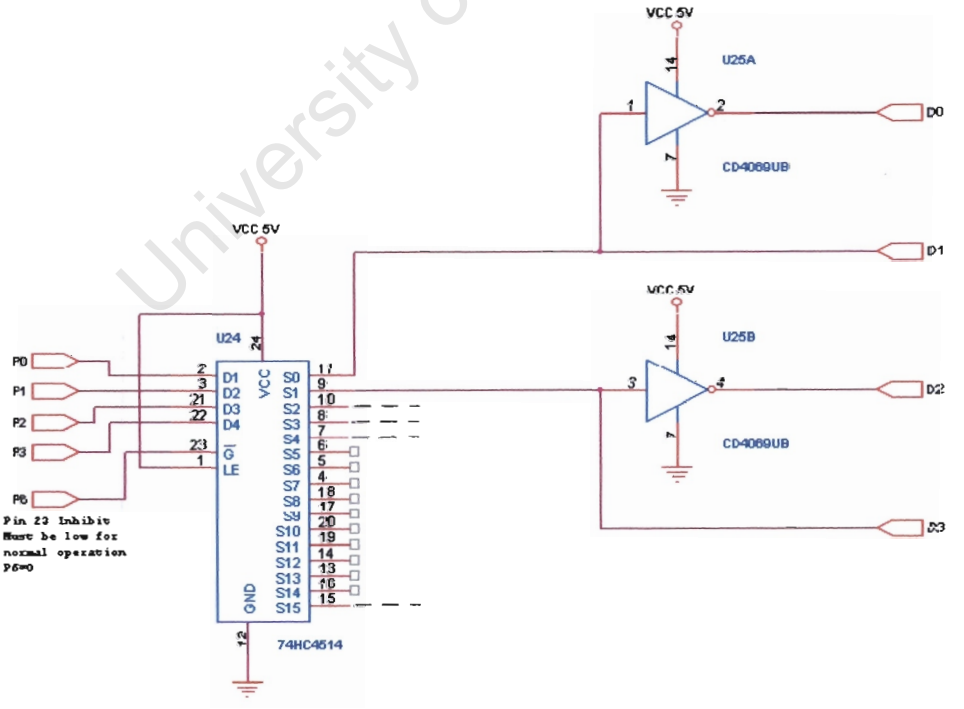

Bibliography

[1] Analog devices, low cost analog multiplier ad633. Technical Report Revision D.

[2] *Polux Principle of Operation.* www.cbs-cbt.com/TECH/PX2/px2_en.html.

[3] *Wikipedia the free encyclopedia.* http://en.wikipedia.org.

[4] Maxim, improved, quad, spst analog switches. dg444/dg445. Technical Report Revision 3, September 2001.

[5] Eskom distribution standard part 11: Maintenance inspection and supplemantal treatment of treated wood utility poles. Technical Report SCSASAAX2, November 2002.

[6] Texas instruments, tl081 jfet-input operational amplfier. Technical report, September 2004.

[7] Case Studies: Materials Technology, www.mbendi.co.za/eskomenterprises/casestudy/case_tsi 16.htm. *In-service Evaluation of Wooden Poles*, eskom enterprises edition.

[8] CBS-CBT. *Sylvatest Information and manual.* http://www.cbs-cbt.com/TECH/index_s_en.html.

[9] R. N. Emerson, D. G. Pollock, J. A. Kainz, K. J. Fridley, D. L. McLean, and R. J. Ross. Nondestructive evaluation techniques for timber bridges. *5th World Conference on Timber Engineering*, 1:670–677, August 1998.

[10] E. Ezer. Measurement of wood pole strength - polux/sup(r)/ anew nondestructive inspection method. *2001 Rural Electric Power Conference, Presented at the 45th Annual Conference, New York, USA*, CAT. no. 01CH37214:c6/1–7, 2001.

[11] J. C. Gamio. A comparative analysis of single- and multiple-electrode excitation methods in electrical capacitance tomography. *Measurement Science and Technology*, 13:1799–1809, June 2002.

[12] J. C. Gamio, W. Q. Yang, and A. L. Scott. Analysis of non-ideal characteristics of an ac-based capacitance transducer for tomography. *Measurement Science and Technology*, 12:1076–1082, April 2001.

[13] A. E. gmbh. *PICUS Sonic Tomograph*. www.argus-electronic.de/english/index.html, May 2003.

[14] Heath Consultants, www.heathus.com. *De-K Tector Brochure*.

[15] P. Horowitz and W. Hill. *The Art of Electronics*. Press Syndicate, 2nd edition, 1989.

[16] IML.inc., www.imlusa.com. *Developer of the Resistograph*, 2003.

[17] H. P. W. J. Reconstruction algorithms. In W. J. G, editor, *Electrical Impedance Tomography*, chapter 10. Adam Hilger, 1990.

[18] E. T. LTD. *Developers of the Pole Ultrasonic Rot Locator*. www.eatechnology.com.

[19] K. H. A. Ltd. *Summary of the Dielectric Permittivity of Wood*. Keam Holdem Industrial RF and microwave technology, www.kha.co.nz/AP-0420.html, July 1999.

[20] D. Naran. Nde of wooden poles. *Eskom Research Report*, RES/RR/00/11679, 2000.

[21] D. of FAKOPP 2D. Fakopp 2d. *FAKOPP Enterprises*, www.fakopp.com.

[22] B. P. Prestage. The in-service nondestructive evaluation of wooden transmission line poles. Masters thesis, University of Cape Town, South Africa, August 1997.

[23] R. Seavey and L. Timothy. Inspection of timber bridges. Technical report, Minnesota Department of Transportation, September 2002.

[24] N. Semiconductor. Lm6164/lm6264/lm6364 high speed operational amplfier.

[25] Sensors and S. Inc. *Developers of the GPR for pole evaluation*. www.sensoft.ca.

[26] Techoline, www.overheadlines.com/technology.html. *Suppliers of Resistograph, Poletest and Polux*.

[27] Tree Solution incorporated, www.sdbca.com/resistograph.htm. *Resistograph Pricing and Range*.

[28] N. B. White. *Development of Phase-Sensitive Electrical Impedance Tomography for the Detection of Decay in Wood*. Phd thesis, UMIST, Manchester, October 1996.

[29] Wilkinson A J, Randall E W, Cilliers J J, Durrett D R, Naido T, Long T M. A 1000-measurement frames/second ERT data capture system with real-time visualization. *IEEE Sensors Journal*, 5(2):300–307, 2005.

[30] P. Williams and T. A. York, editors. *Evaluation of Integrated Electrodes for Electrical Capacitance Tomography*, Buxton, Greater Manchester, April 1999. 1st World Congress on Industrial Process Tomography.

[31] W. Q. Yang. Hardware design of electrical capacitance tomography systems. *Mesurement Science and Technology*, 7:225–232, September 1996.

[32] W. Q. Yang. Further developments in an ac-based capacitance tomography system. *Review of Scientific Instruments*, 72(10):3902–3907, October 2001.

[33] W. Q. Yang and T. A. York. New ac-based capacitance tomography system. *IEE Proceedings - Science and Measurement Technology*, 146(1):47–53, January 1999.